# Characterizing lithological, weathering, and hydrothermal alteration influences on volcanic rock properties via spectroscopy and laboratory testing: a case study of Mt. Ruapehu volcano, New Zealand

Lauren N. Schaefer[1], Gabor Kereszturi[2], Ben Kennedy[1], Marlène Villeneuve[3]

[1]Earth and Environment, University of Canterbury, Private Bag 4800, Christchurch, New Zealand
[2]Volcanic Risk Solutions, School of Agriculture and Environment, Massey University, Private Bag 11 222, Palmerston North, New Zealand
[3]Montanuniversität Leoben, Leoben, Austria

**Abstract:** The geomechanical characterization of volcanic material has important implications for geothermal and mineral exploration, engineering design, geophysical signals of volcano unrest, and models of instability and mass flows. Chemical weathering and hydrothermal systems can alter the host rock, leading to changes in mechanical behavior and failure mode. Here, we compare the physical and mechanical properties of lava, autoclastic breccia, and pyroclastic (scoria) rocks from Mt. Ruapehu volcano in New Zealand to mineralogical composition determined via infrared spectroscopy and scanning electron microscopy (SEM) with energy-dispersive X-ray spectroscopy (EDS). Laboratory-based spectroscopy shows that the samples contain absorption features indicative of Al-rich hydrous phyllosilicates, Fe- and Mg-rich varieties, and sulfates attributed to surface weathering, supergene, and steam-heated alteration. We find that porosity and primary lithology (i.e., rock origin) are the predominant control on physical and mechanical properties, followed by the pervasiveness of weathering/alteration, and then mineralogical composition. Several properties, such as porosity, uniaxial compressive strength, P-wave seismic velocity, density, and Young's modulus, show strong correlations with other properties, indicating the potential for transfer functions between these properties. Rocks near the active hydrothermal system with high intensity hydrothermal alteration do not follow typical physical and mechanical property trends due to high clay content, low permeability, and low strength. The presence of these rocks within the edifice at Mt. Ruapehu implies local barriers to fluid flow and subsequent pore pressure variations. Additionally, material in the upper conduit area of Mt. Ruapehu may be over two times weaker than typical porosity-strength trends observed in surface rocks, increasing the likelihood of structural failure. Trends in the pervasiveness of weathering with physical and mechanical properties, along with shifts in the position of spectral absorption peaks as hydrothermal/weathering alteration increases, suggest that it may be possible to extrapolate properties from imaging spectroscopy.

**Keywords**: uniaxial compressive strength, permeability, porosity, triaxial compressive strength, intact rock $m_i$, andesite, failure mode, hydrothermal alteration, weathering, argillic alteration

## 1. Introduction

Chemical weathering and hydrothermal alteration influence the physical and mechanical properties of volcanic rock, with implications for geothermal and epithermal mineral resources (e.g., Heap et al., 2019a), the use of volcanic material in the construction industry (Yildiz et al., 2010), failure modes and the evolution of rock physical properties (Heap et al., 2015c), and volcano structural stability (Watters et al., 2000). In active volcanic environments, rock properties are critical for modeling instability or mass flows, and interpreting geophysical signals of volcano unrest (e.g., volcano-seismic or geodetic; Reid et al., 2001; Mordensky et al., 2019a; Heap et al., 2020; Hickey et al., 2020). Inherent heterogeneities in volcanic primary material create physically and mechanically varied structures (Mordensky et al., 2018; Saubin et al., 2019). These heterogeneities are exacerbated by the circulation of hydrothermal fluids and/or chemical weathering under widely varying temperature, chemical, temporal, and spatial conditions. These processes result in mineral oxidation, dissolution, replacement, and/or precipitation that variably alter the physical and mechanical properties of the volcanic host rock (e.g., Reid et al., 2001; Dobson et al., 2003; Ball et al., 2013; Siratovich et al., 2014; Wyering et al., 2014; Mordensky et al., 2018, 2019a, 2019b; Farquharson et al., 2019; Heap et al., 2019a, 2019b; Kennedy et al., 2020). For example, weathering and alteration can decrease or increase porosity and permeability of volcanic rock depending on the nature of the host rock, the fluid type and composition, temperature, and the duration of rock-fluid interaction (Frolova et al., 2015; Farquharson et al., 2019; Mordensky et al., 2019b; Villeneuve et al., 2020). Changes in these properties in turn influence fluid flow, strength, and the deformation response of rock masses. A considerable presence of clays due to hydrothermal alteration has been attributed to large-scale volcano collapses (López and Williams, 1993; Crowley and Zimbelman, 1997), supported by numerical simulations of collapse scenarios (Reid et al., 2001; Ball et al., 2018).

Here, we explore the influence of weathering and hydrothermal alteration on the physical and mechanical properties of lava, autoclastic breccia, and pyroclastic (scoria) rocks from Mt. Ruapehu, an active andesitic stratovolcano in New Zealand. Mt. Ruapehu is a glaciated volcano with both an active and relict hydrothermal systems that are variably exposed at the surface, resulting in a variety of fresh, weathered, and hydrothermally altered material (Townsend et al., 2017). Rock alteration mineralogy is determined using a combination of infrared spectroscopy and scanning electron microscopy (SEM) with energy-dispersive X-ray spectroscopy (EDS). Infrared spectroscopy collects information from hundreds of narrow and contiguous spectral bands in the visible (400-700 nm), near-infrared (NIR; 700-1000 nm) and shortwave infrared (SWIR; 1000-2500 nm) wavelengths, capable of identifying chemical characteristics of materials using indicator minerals with characteristic absorption features (van der Meer, 2018). Many indicator minerals are common weathering, oxidation, and hydrothermal alteration products in volcanic environments. For example, iron is highlighted in the NIR region, useful for detecting minerals such as goethite, hematite and jarosite (Zimbelman et al., 2005). Al-, Fe-, Mg-, -OH, -$SO_4$, -$CO_3$ and -$H_2O$-bearing minerals can be detected in the SWIR region, identifying minerals such as alunite, gypsum, anhydrite, topaz, muscovite, biotite, epidote, calcite, dolomite, and clay minerals (Hunt and Ashley, 1979; Swayze et al., 2014; Neal et al., 2018). Infrared spectroscopy can also be sensitive to other mechanically relevant rock microstructure properties such as grain size and crystallinity (Clarke, 1999; Ruitenbeek et al., 2019; Okada et al., 2020).

The aims of this paper are to: (1) produce a spectroscopic and petrologic description of the fresh, weathered, and hydrothermally altered rock of Mt. Ruapehu volcano, (2) physically and mechanically characterize these rocks, and (3) examine the relationships between physical and

mechanical properties and the type and extent of weathering and hydrothermal alteration. Mineralogical-physical-mechanical relationships will help to develop geotechnical models of volcanic and geothermal systems, and guide numerical simulations of volcanic hazards.

## 2. Materials and methods

### *2.1 Study area and materials*

Mt. Ruapehu is a complex andesitic composite volcano located in the Taupo Volcanic Zone of the central North Island of New Zealand (Figure 1). The volcano is frequently active, with several historic small-to-moderate explosive eruptions and lahar events (Scott, 2013). The oldest geologic rocks are 250 ky old, and were exposed to glaciation up until 10 ky ago (Hackett, 1985), and the youngest fresh magmatic rocks were erupted in 1996 (Nakagawa et al., 1999). The stratigraphic framework of Mt Ruapehu comprises four formations, on the basis of geochronology, geochemistry and stratigraphic relationships, pinpointing distinct spatial-temporal stages of volcano evolution (Figure 1): Te Herenga (200 to 150 ka), Wahianoa (166-80 ka), Mangawhero (50-15 ka) and Whakapapa (<15 ka) formations (Hackett and Houghton, 1989; Price et al., 2012; Conway et al., 2016; Townsend et al., 2017, Figure 1c). The volcano has an active hydrothermal system underneath the summit vent that hosts a crater lake (Christenson and Wood, 1993). Older hydrothermal systems are also variably exposed at the surface around the summit plateau (Figure 1b). This varied geological, glacial, and hydrothermal history results in a wide variety of fresh, weathered, and altered material.

Sampling locations were partially directed by aerial hyperspectral imagery collected using a push-broom, VNIR-SWIR AISAFenix imaging system, flown in March of 2018 (Kereszturi et al., 2020b; Miller et al., 2020, Figure 1b). A total of 23 blocks of lava, autoclastic breccia, and pyroclastic (scoria) rocks varying from fresh to pervasively altered were selected to represent the variability of the physical properties of the material forming the volcanic edifice (Figs 1-2, Table 1). The blocks had a volume of c. 8000 $cm^3$ (typical edge length of 20 cm), and were large enough to obtain all of the test specimens of a given rock type from the same piece. Each block was inspected for macroscopic defects so that it would provide test specimens free from fractures, seams, partings, or joints. Block sample names follow the same nomenclature as (Kereszturi et al., 2020). All blocks are considered surface samples excluding RH50; RH50 is a block from the 1995-1996 eruption that represents lava from the upper conduit area within the current vent hosted hydrothermal system (Kilgour et al., 2010), and thus is considered a subsurface sample. Pyroclastic sample RH15 is a block of scoria located in an undifferentiated tephra fall deposit. The term 'sample' refers to the 23 rock blocks, while cores or pieces from each block are referred to as 'specimens' throughout.

### *2.2 Laboratory spectroscopy and Scanning Electron Microscopy (SEM)*

Each of the 23 blocks listed in Table 1 was measured using an ASD FieldSpec® 4 Hi-Res NG spectroradiometer, which recorded 2151 spectral bands between 350 and 2500 nm. This instrument has a full-width-half-maximum (FWHM) of 3 nm at 700 nm and 8 nm at 1400-2100 nm regions. The spectral bandwidth is 1.4 nm between 350-1000 nm, as well as 1.1 nm between 1001 and 2500 nm. Spectral data were captured using a High Brightness contact probe with a halogen light illumination source. The contact probe has a measurement spot size of 10 mm. Each measurement was calibrated using a white Spectralon® Diffuse Reflectance Standard. Both freshly chipped surfaces (sample interior) and the exterior of the sample were measured for a total of 3-5 spectral readings per block. Phenocrysts are typically 1 mm or smaller (Figure 3), therefore the

contact probe size, being 10 times larger than the average phenocryst size, was sufficient to capture the spatial heterogeneity in each block. See Danner et al. (2015) for FieldSpec schematic and spectral sampling details.

Inherent variation in detector sensitivity and variations in temperature conditions can cause spectral drift at two wavelength locations where detector arrays meet (e.g., VNIR and SWIR). These drifts were corrected by applying a splice correction function using the ASD View Spec Pro software (Danner et al., 2015). The splice correction function considers the average of tangents at either side of a break point to determine the new points through which the line passes without drift (see Danner et al. (2015) for schematic and details). The splice-corrected spectral readings for each block were then averaged. The spectral data were then normalized using a convex hull continuum removal method. The continuum is a convex "hull" of straight-line segments fitted over the top of the spectrum that connect local spectral maxima. The continuum is removed by dividing the original reflectance value by the corresponding values of the continuum line (convex hull) at a given wavelength. Removing this continuum standardizes isolated absorption features for comparison between samples (Kokaly and Clark, 1999; Huang et al., 2004).

The sample mineralogy was further constrained using a ThermoFisher Scientific™ FEI Quanta 200 Environmental Scanning Electron Microscope (SEM) operated in Back-Scattered Electron (BSE) mode under accelerating voltage of 20 kV, with a working distance of 10 mm, at Massey University's Manawatu Imaging Centre. Minerals were recognized based on their textural and crystal habits as well as using Energy-dispersive X-ray Spectroscopy (EDS) (Shindo and Oikawa, 2002; Severin, 2004).

### *2.3 Laboratory physical and mechanical measurements*

The 23 blocks were cored to create several specimens per block (5 to 8) with a diameter of 20 mm, and then ground to a length:diameter ratio of 2-2.15:1. See Supplementary Table for details of each specimen. For each specimen, we measured porosity, permeability, and compressional (Vp) and shear wave (Vs) velocity (Section 2.3.1 and 2.3.3). Dynamic Young's modulus and dynamic Poisson's ratio were calculated from Vp and Vs results (Section 2.3.3). Porosity, permeability, Vp, Vs, dynamic Young's modulus, and dynamic Poisson's ratio values were then averaged for each block. Magnetic susceptibility was measured on the natural face and a cut face of each block and averaged to produce one value of magnetic susceptibility per block (Section 2.3.2). Two to three specimens from each block were then used for uniaxial compressive strength (UCS) experiments, from which static Young's modulus values were calculated (Section 2.3.4). UCS and static Young's modulus were also averaged to produce a single value for each block. Another three specimens from each block were used for triaxial compressive strength testing. Triaxial results were used to calculate friction angle, cohesion, and the Hoek-Brown material constant for intact rock ($m_i$) for each block (Section 2.3.5). All specimens were oven-dried at 60°C for a minimum of 48 hours and then allowed to cool to room temperature prior to testing.

All physical and mechanical property testing was conducted at the University of Canterbury rock mechanics laboratory. The physical and mechanical properties measured and examined in this study are commonly used to develop models of fluid flow (e.g., porosity, permeability; e.g., (Day, 1996; Gonnermann and Manga, 2007; Kennedy et al., 2020), slope failure (e.g., UCS, friction angle, cohesion, material constant for intact rock $m_i$; e.g., Apuani et al., 2005; Schaefer et al., 2013; Heap et al., 2021; Wallace et al., 2021), subsurface imaging, and monitoring deformation and geophysical phenomena such as seismicity (e.g., Young's modulus, Poisson's

ratio, Vp, Vs, density, magnetic susceptibility; e.g., (Lu et al., 2005; Mordensky et al., 2019a; Heap et al., 2020).

Pearson's correlation coefficient (PCC or Pearson's *r*) and Spearman's rank correlation coefficient (SCC or Spearman's $\rho$) were used to correlate one physical or mechanical property (X) to another physical or mechanical property (Y). Pearson's correlation coefficient is the measure of the linear correlation between two variables as:

$$PCC\ (r)_{X,Y} = \frac{cov(X,Y)}{\sigma_X \sigma_Y} \quad (1)$$

where cov is the covariance, $\sigma_X$ is the standard deviation of X and $\sigma_Y$ is the standard deviation of Y. Spearman's rank correlation coefficient is the measure of the monotonic correlation between two variables. For a sample size of *n*, the *n* raw scores $X_i$ and $Y_i$ are converted to ranks $R(X_i)$ and R(Y ), and SCC is computed as:

$$SCC\ (\rho)_{R(X),R(Y)} = \frac{cov(R(X),R(Y))}{\sigma_{R(X)} \sigma_{R(Y)}} \quad (2)$$

where the cov is the covariance of the rank variable, and the $\sigma_{R(X)}$ and $\sigma_{R(Y)}$ are the standard deviation of the two rank variables being compared. The correlation coefficient values (*r* or $\rho$) range from -1 to 1, with '-1' indicating a total negative correlation between variables, '0' indicating no relationship, and '1' indicating a total positive relationship.

*2.3.1 Porosity, density, and permeability*

Oven dried specimens were used for measuring dry mass, dry density, unit weight, porosity, and permeability. Porosity was measured using a Micromeritics AccuPyc™ II 1340 helium pycnometer, which measures the specimen's solid volume ($V_s$). This is subtracted from the total volume ($V_t$) to determine pore volume ($V_p$) and connected porosity ($\varphi$), as follows: $V_t$-$V_s$=$V_p$, and $\varphi$=$V_p$/$V_t$. Specimen density was calculated by dividing the mass of each specimen by its total volume ($V_t$).

For relatively high permeability specimens (>$10^{17}$ $m^2$), permeability was measured at room temperature using a steady-state Vinci Technologies benchtop permeameter interfaced with a Bronkhorst El-Flow® volumetric flowmeter. The steady state permeameter records the volumetric flow rate through the specimen core, driven by the pressure differential of nitrogen as the pore fluid upstream, and ambient atmospheric pressure downstream. Specimens were placed in a rubber sleeve in a Hoek cell and radially confined at 1 MPa prior to applying nitrogen gas at a steady pressure to one end of the sample. The radial confinement assured that the nitrogen gas flowed through the specimen and not between the sample edge and the membrane. See Hill (2020) for steady state permeameter setup details. Flow rate measurements were collected at several pressure gradients, allowing permeability to be calculated using Darcy's Law:

$$-\frac{dp}{L} = \frac{(\mu Q)}{A k_D} \quad (3)$$

where *p* is the pressure, *L* is the length of the specimen, A is the cross-sectional area, $k_d$ is the gas permeability, $\mu$ is the dynamic viscosity coefficient of the pore fluid, and *Q* is the flow rate.

For lower permeability specimens (<$10^{-17}$ $m^2$), permeability was measured using a Core Laboratories PDP-200 pulse decay permeameter at 30°C . Specimens were placed in a core holder

and a uniform confining pressure of ~2 MPa was manually applied with a hydraulic pump to assure that the test fluid moved through the specimen and not between the specimen and the core holder. The system uses nitrogen gas to saturate the test specimen and then the downstream gas valve is opened, allowing for a pressure differential to develop across the specimen. The system then measures the pressure differential decay across a specimen at regularly timed intervals. Permeability was calculated through a function provided in Brace et al. (1968) as follows:

$$k_{gas} = \left(\frac{2\eta L}{A}\right)\left(\frac{V_{up}}{p_{up}^2 - p_{down}^2}\right)\left(\frac{\Delta p_{up}}{\Delta t}\right) \quad (4)$$

where $k_{gas}$ is gas permeability, $\eta$ is the viscosity of the pore fluid (nitrogen), $\Delta t$ is change in time, $L$ is the length of the specimen, $A$ is the cross-sectional area of the specimen, $V_{up}$ is the volume of gas in the upstream reservoir and piping, $p_{up}$ is the pressure of the gas in the upstream reservoir and piping, $p_{down}$ is the pressure of gas in the downstream reservoir and piping, and $\Delta p_{up}$ is the change in $p_{up}$ during the elapsed time. See Cant et al. (2018) for pulse-decay permeameter setup details.

*2.3.2 Magnetic susceptibility*

Magnetic susceptibility was measured using a Terraplus KT-10 v2 magnetic susceptibility meter on the natural face and a cut face of each block. The KT-10 meter was held in direct contact with either the natural or cut surface of the block in accordance with the manufacturer (see Terraplus User's Guide, v. 2.1), measured three times, and averaged to produce one value per block. Measurements were not made on individual specimens due to the 65 mm coil diameter in the KT-10 meter.

*2.3.3 Elastic wave velocities and dynamic elastic moduli*

Dry compressional (Vp) and shear wave velocities (Vs) were collected using a GCTS CATS interfaced with transducer-mounted piezoelectric quartz crystals operating at a 900 kHz resonance frequency and a 20 MHz pulse sampling rate, with a minimum of 100 waveforms per compression wave type per specimen. Ultrasonic gel and a constant 312 Pa stress were applied to ensure sufficient contact between the specimens and platens to produce consistent waveforms. Dynamic Young's modulus and dynamic Poisson's ratio were calculated as follows (Guéguen and Palciauskas, 1994)

$$\nu_d = \frac{V_P^2 - V_S^2}{2(V_p^2 - V_s^2)} \quad (5)$$

$$E_d = \frac{\rho V_s^2\left(3V_p^2 - 4V_s^2\right)}{\left(V_p^2 - V_s^2\right)} \quad (6)$$

where $\nu_d$ is the Poisson's Ratio, $V_p$ is compressional wave velocity, $V_s$ is shear wave velocity, $E_d$ is the Young's Modulus, and $\rho$ is dry bulk density.

*2.3.4 Uniaxial compressive strength and static Young's modulus*

Dry uniaxial compressive strength (UCS) measurements were conducted on a Technotest 3000 kN servo-controlled loading frame at room temperature. Specimens were tested at a constant

strain rate of 1.0 x $10^{-5}$ $s^{-1}$, similar to other studies of volcanic material (Siratovich et al., 2014; Heap et al., 2015b; Schaefer et al., 2015; Mordensky et al., 2018). Axial strain was measured using a linear-variable displacement transducer extensometer, and static Young's modulus was determined using the average modulus of the linear portion of the stress-strain curve following ASTM standards (ASTM D7012-07).

*2.3.5 Triaxial compressive strength, friction angle, cohesion, and intact rock constant $m_i$*

Three specimens from each block were tested in conventional triaxial conditions ($\sigma_1' > \sigma_2' = \sigma_3'$, in which $\sigma_1'$ is the major effective principal stress, $\sigma_2'$ is the intermediate effective stress, and $\sigma_3'$ is the minor effective principal stress) over a limited range of confining stresses ($\sigma_3'$), with no confining stress larger than 50% of the average UCS of the block (as determined using by calculating the average UCS of specimens tested from the same block) to ensure that failure remains in the brittle regime (Labuz and Zang, 2012; Hoek and Brown, 1980; Hoek and Brown, 1997). Dry triaxial compressive strength measurements were conducted using a Hoek cell and deformed with a Technotest 3000 kN servo-controlled loading frame at a constant strain rate of 1.0 x $10^{-5}$ $s^{-1}$ at room temperature. Common confining stresses of 2, 3, 5, 10, 20, 22, or 25 MPa were used when possible, to allow for comparison between samples. Results from the triaxial laboratory experiments were analyzed with the Rocscience RSData software to calculate material constant $m_i$, friction angle and cohesion for each block. The material constant $m_i$ was calculated using the Hoek-Brown failure criterion for intact rock with the modified cuckoo curve fitting method and basic error summation method (see Supplementary Material for RocData processing results). Friction angle and cohesion were calculated using the linear curve fitting method and vertical error summation method (see Supplementary Material for RocData processing results).

## 3. Results

### *3.1 Alteration mineralogy and classification*

The laboratory-based spectroscopy results show that the blocks contain distinct absorption features around 1410-1450 nm, 1920 nm, and within the broader spectrum between 2180-2400 nm (Figure 3A), indicating the presence of phyllosilicates including kaolinite, halloysite, smectites (mostly montmorillonite and nontronite), and minor illite (Laukamp et al., 2021). The samples also occasionally contain minor absorption features around 2180 and 2265 nm, which are due to the presence of alunite and jarosite, respectively (Figure 3A). More commonly, the samples have absorption features in the visible region, notably around 390, 425, 485, and 540 nm, which are consistent with minerals such as sulfur, goethite, and hematite (Figure 3A). Based on SEM-EDS analysis, some samples have disseminated pyrite, occurring together with silica polymorphs (e.g., RH28, RH38, Figure 3D, E). These minerals do not have any strong characteristic absorption features in the visible and shortwave-infrared regions. Alteration minerals are often limited to vugg- and fracture infills and occur as partial to full replacement of the original mineralogy (Figure 3D, E). A detailed characterization of sample alteration mineralogy, including a conceptual model of alteration history at Mt. Ruapehu, is described in detail in (Kereszturi et al., 2020).

Following the weathering/alteration assemblages, defined by indicator minerals (minerals specific to certain weathering, oxidation, and hydrothermal alteration processes), their occurrence, and their origin (Rye, 2005; Simmons et al., 2005) samples were categorized into four mineral assemblages (Table 2): (1) Fresh, consisting of primary mineralogy such as pyroxene, plagioclase, and titanomagnetite; (2) Surface weathering, consisting of primary and chemically weathered and oxidized minerals including Fe-oxides (hematite) and minor smectites typically occurring in a

weathered rim; (3) Supergene, argillic alteration that develops at <40°C through long-term weathering and oxidation of ferrous and minor sulfide-bearing rocks in atmospheric conditions, which includes phyllosilicates, jarosite, and Fe-oxides; (4) Steam-heated, intermediate and advanced argillic alteration that develops at <120°C near the water table and in the shallowest epithermal environment, including, quartz, pyrite, Fe oxides (goethite), phyllosilicates, sulfur, and occasional jarosite and alunite (Table 2). The latter two categories often show mineral imprinting, when rocks subjected to hypogene conditions are later subjected to weathering and erosion, resulting in the replacement of some meta-stable hydrothermal minerals (e.g., pyrite) in atmospheric pressure and temperature conditions.

In addition to various mineral assemblages, samples also showed variations in alteration pervasiveness. Thus, samples were also categorized into four groups based on the extent of weathering/alteration, including "none" (fresh material), "minor" (typically only the exterior/crust of the sample is weathered or altered), "moderate" (weathering or alteration is present throughout the groundmass), and "pervasive" (weathering or alteration is strongly present in groundmass and crystals) (Table 3). Surface weathering samples have varying percentages of total weathered material, with autoclastic breccias (e.g., samples RH4, RH6) and the tephra (RH15) being more pervasively weathered than lavas (e.g., samples RH2b, RH2, RH5, RH8, RH10, RH16) due to preexisting fractures, smaller grain size, and more void space.

### *3.2 Physical and mechanical characterization*

Block averaged properties are shown in Table 3, apart from triaxial compressive strength results, which are shown in Figure 4 and summarized in Table 4. Properties for each specimen (individual cores) are available in the Supplementary Table. Correlation coefficients for both Pearson's and Spearman's rank between material properties for all blocks are shown in Figure 5. Additional results are presented as graphs of individual parameters plotted against either porosity (Figure 6 and Figure 7) or Vp (Figure 8), which systematically have the highest correlation factors to other physical and mechanical properties (Figure 5). Volcanic "lithology" is used to categorize rocks by their physical characteristics (e.g., texture) as a result of the origin of the rock/deposit, resulting in the categories of 'lava', 'autoclastic breccia' and 'pyroclastic' rock.

Porosity, permeability, density, and magnetic susceptibility results are as follows:

-The average connected porosity of specimens ranges from 1.6-48.3%, highlighting the heterogeneity of the sample suite (Figure 2).

-Porosity is generally higher in autoclastic breccias and pyroclastic rocks (c. 22-48 %) than lavas (c. 2-30 %) (Figure 6A).

-Porosity is highest in rocks with surface weathering (average = 18%) (Figure 6B) and pervasive alteration (average = 28%) (Figure 6D).

-The standard deviation of porosity between specimens is below 2%, except for RH6 (SD = 3%) and RH19 (SD = 3.2%).

-Specimen dry mass density generally increases with decreasing values of porosity, ranging from 1.37 to 2.67 g/cm$^3$.

-Permeability exhibits 6 orders of magnitude difference between the lowest ($4x10^{-18}$ m$^2$) and highest ($3x10^{-12}$ m$^2$) permeable specimens.

-Lavas typically have lower permeability ($<1x10^{-14}$ m$^2$) than autoclastic breccias and pyroclastic rocks ($>1x10^{-14}$ m$^2$) (Figure 7A). Despite this trend, the permeability of rocks with similar porosities can vary by up to two orders of magnitude.

-Magnetic susceptibility ranges from 0 to 0.04 SI, with a weak relationship with porosity (Figure 7D-F).
-Pervasively altered and steam-heated blocks have lower magnetic susceptibility than less altered or unaltered blocks, and lavas have higher magnetic susceptibility than autoclastic breccias and pyroclastic rocks.

Dry Vp and Vs are inversely related to porosity, with notably higher Vp and Vs velocities in lavas than autoclastic breccias and pyroclastic rocks (Figure 7M-O, 8A); all lava Vp are > 3600 m/s and Vs are > 1300 m/s, while autoclastic breccias and pyroclastic rocks have Vp <3400 m/s and Vs <1400 m/s, with the exception of RH42b with a Vs of 1661 m/s. Vp and Vs are lowest in pervasively altered samples, but do not systematical vary with alteration pervasiveness or alteration type (Figure 8B-C). Similar patterns exist for dynamic Poisson's ratio and dynamic Young's modulus, which range between 0.23-0.46 and 7.1-32.1 GPa, respectively. Static Young's modulus shows a wider range than dynamic Young's modulus, varying between 3.7-42.3 GPa. Again, static Young's modulus is significantly higher in lavas (average = 23 GPa) than autoclastic breccias and pyroclastic rocks (average = 7.5 GPa), is closely dependent on porosity (Figure 7G-I), shows weak systematic decreasing trends with increasing alteration type and pervasiveness, and has a strong relationship to Vp (Figure 8D-F). Dynamic Young's modulus values tend to be higher than static Young's modulus, although this is reversed for stiffer material (values > 25 GPa) (Figure 9).

Uniaxial compressive strength (UCS) correlates with porosity (Figure 5), with UCS decreasing exponentially with increasing porosity (Figure 6). In lower porosity samples (<10%), UCS can vary by over 200 MPa. Variations in UCS for samples with >10% porosity are much smaller (~50 MPa max). UCS at low porosity (< 20%) decreases with an increase in the pervasiveness of weathering or hydrothermal alteration, and fresh material is stronger than surface weathering and supergene alteration, all of which are stronger than steam-heated material. Again, there can be large ranges of UCS values within these alteration categories, and the trends described do not apply to material >= 20% porosity.

Triaxial experiments show that sample strength increases with increasing confining pressure (Table 4, Figure 4E, F). Stress-strain curves show that fresh and altered lava samples exhibit brittle mechanical behavior (Figure 4A) at low confinement, where a peak stress (differential stress) is reached followed by strain softening (as described in Wong and Baud, 2012). While fresh breccias also display brittle mechanical behavior at low confinement, altered breccias display ductile behavior (Figure 4B), characterized by an absence of strain softening and dilation, and where failure is a function of compactant pore collapse (as described in Heap et al., 2015a). Unaltered lavas tend to be strong, stiff and with low porosities, while altered lavas tend to be weak, ductile or have high porosities (Figure 4A-B, E-F), and samples with similar porosities tend to have similar strength values at a given confining pressure (Figure 4C, 4D). Altered samples tend to reach lower peak stress, have a less defined failure peak, or experience higher strains than fresh samples (Figure 4A-B, E-F), although deviations from these patterns do occur.

Cohesion covers a wide range of values from 1.8 to 52.4 MPa (Table 3), which has a positive correlation with UCS (Figure 5a) and a positive logarithmic relationship with Vp (Figure 8G-I). Like UCS, cohesion is higher in lavas than autoclastic breccias and pyroclastic rocks, and decreases with increasing weathering and alteration pervasiveness. Friction angle ranges from 37 to 57° (Table 3), and has a positive and monotonic (in this case logarithmic) relationship with intact rock parameter $m_i$ (Figure 5b). Intact rock parameter $m_i$ ranges from 6 to 48 (Table 3) and

has a weakly negative monotonic correlation with porosity (Figure 5b), but no clear relation to rock texture, alteration type or pervasiveness when plotted against porosity (Figure 7).

## 4. Discussion

### *4.1 Weathering and alteration mineralogy*

The weathered/altered minerals identified by infrared spectroscopy are predominately Fe-bearing oxides and clay mineral associations typical of acid-sulfate alteration processes, producing argillic to advanced argillic alteration of the primary volcanic rocks (Heald et al., 1987; Simmons et al., 2005). The alteration minerals form through supergene to hypogene weathering and/or alteration of the host rocks that originally contain plagioclase, minor pyroxene, (titano-)magnetite, and rarely olivine, amphibole phenocrysts and microcrystals in the groundmass (Figure 3). These mineral associations are consistent with acidic and steam-heated environments, such as the currently active vent-hosted system underneath Mt. Ruapehu's Crater Lake (Christenson and Wood, 1993; Christenson, 2000), which leads to formation of sulfides and sulfates from the oxidation of $H_2S$ and $H_2SO_4$-rich fluids by atmospheric oxygen at shallow depths.

Samples show a strong shift in the position of the $Fe^{3+}$ iron absorption from 530 nm (e.g., hematite-dominated) to shorter wavelengths around 480 nm (e.g., goethite-dominated), as hydrothermal/weathering alteration increases (Figure 3). This spectral shift is indicative of the pH preference of these indicator minerals (e.g., hematite-dominance in less-acidic and neutral pH conditions; Schwertmann and Murad, 1983) and the presence of disseminated pyrite formed through acid-sulfate alteration, which may later undergo supergene oxidation, resulting in the formation of Fe-oxides (goethite), jarosite, gypsum, and smectite (Rye, 2005). Spectral peaks at 2160-2210 nm, 2315 nm, and 2390 nm for samples with increased clay content (e.g., kaolinite, smectites) are associated with longer exposures to weathering or hydrothermal fluids. This is consistent with the present-day geology of Mt. Ruapehu, where ancient hydrothermal systems can be partially covered by younger volcaniclastic and lava rocks (e.g., Kereszturi et al., 2020).

### *4.2 Physical and mechanical property relations*

Physical and mechanical test results reveal several common relations between material properties (Table 3-4, Figure 4-9). Similar to other studies, we find that porosity has a first-order effect on other physical and mechanical properties, including strength and stiffness, permeability, and rock failure mode (Al-Harthi et al., 1999; Pola et al., 2012; Heap et al., 2014a, 2014b, 2015b, 2019a; Schaefer et al., 2015; Siratovich et al., 2016; Cant et al., 2018; Coats et al., 2018; Mordensky et al., 2018). UCS and Young's modulus decrease exponentially with increasing porosity, while permeability increases exponentially with porosity (Figures 6 and 7). Low porosity samples also generally have higher values of Poisson's Ratio, $m_i$, magnetic susceptibility, and Vp velocities. Lavas typically have lower porosities (< 20%) than autoclastic breccias and pyroclastic rocks (> 20%) due to emplacement mechanisms; the slow cooling of lava flows allows gas bubbles to escape prior to solidification resulting in lower porosity, while the rapid cooling of pyroclastic rock traps gas bubbles resulting in higher porosity). Thus, lithology (i.e., lava, autoclastic breccia, or pyroclastic rocks) additionally correlates to material properties (Figure 6, Figure 7, Figure 8; as in Mordensky et al., 2018). However, it should be stressed that within each of these categories, properties can vary significantly. For example, in low porosity samples (lavas with porosity <10%), UCS can vary by over 200 MPa. Even within 6-7% porosity, sample peak stress can vary by 100 MPa (Figure 4C).

Vp, density, and Young's modulus also show strong relationships with many material properties (Figs. 5 and 7). Seismic velocities in volcanic rocks typically attenuate with the presence of glass, clay alteration, microcracks, and vesicles (e.g., Vanorio et al., 2002; Pola et al., 2012). Similar to other authors (e.g., Wyering et al., 2014), we find that the correlations between Vp and porosity, density, and permeability are strong. Correlations of Vs with other properties is weaker than Vp, likely because of errors related to the difficulty in picking the first arrival of the S-wave, leading to a large dispersion of Vs values. Static Young's modulus also correlates well with Vp, density, and strength (Figure 5). Density, and dynamic Poisson's ratio and Young's modulus calculated from seismic velocities, show similar but weaker relations compared to static Young's modulus (Figure 5), likely arising from the dispersion of Vs. We find that magnetic susceptibility correlates moderately with Young's modulus (Figure 5) and porosity (Figure 7), although the relationship with Young's modulus may be the result of porosity rather than a truly independent relationship. The relation of magnetic susceptibility with porosity may stem from the oxidation and alteration of magnetic minerals, along with lower porosity, non-magnetic clay minerals replacing primary magnetic minerals (e.g., titanomagnetite). The relationship of magnetic susceptibility with other material properties is generally moderate to weak (Figure 5, Figure 7 D-F), although lavas tend to have higher magnetic susceptibility values than autoclastic breccias and pyroclastic rock.

Friction angle and $m_i$ correlate well to each other, as expected since they represent the slope and curvature of the failure criteria, respectively, but not to any other parameters (Figure 5), except for porosity (Figure 7 and (Villeneuve and Heap, 2021). Cohesion correlates to UCS as expected since they both describe the low-confinement strength components of the failure criteria, as well as density, Young's modulus (Figure 5) and Vp (Figure 8), and porosity, as also shown in (Villeneuve and Heap, 2021). This is the first research that attempts to link $m_i$ to alteration and weathering of volcanic rocks. Although $m_i$ has been thoroughly studied for other crystalline and sedimentary rocks (e.g., Cai, 2010; Richards and Read, 2011; Carter, 2020), most of these studies focus on deriving $m_i$ from lab data or novel methods for estimating it using rock texture (e.g., porosity). Richards and Read (2011) provide a clear discussion regarding the wide variability of this parameter, and this research highlights that, although all of the tested samples are andesite, they vary considerably in terms of their texture and mineralogy, leading to a wide range of $m_i$. (Villeneuve et al., 2021) and (Villeneuve and Heap, 2021) show that for these rock types, where triaxial data are not available, porosity is a potential indicator of $m_i$ (as also shown in Figure 7), however the wide variation of $m_i$ for a given porosity highlights that $m_i$ depends on several factors, in addition to porosity. As with strength, $m_i$ tends to be higher for fresh rocks than for weathered and altered rocks, which is most pronounced for low-porosity lava (Figure 10). This shows that more research is required to decipher the links between failure criterion parameters and physical characteristics to improve on empirical data and provide reliable means to estimate these parameters in the absence of triaxial testing, as is often the case in volcano studies.

### *4.3 The influence of weathering and alteration on physical and mechanical properties*

While the extent of altered or weathered minerals is in large part due to historic conditions, we find that lavas are less pervasively weathered/altered than autoclastic breccias and pyroclastic rocks (Figure 6A and 6D). In addition to having more void space, autoclastic breccias and pyroclastic rocks also have more incipient micro-fractures (Mordensky et al., 2018), both of which increase permeability (Figure 7 A-C) and surface area (Farquharson et al., 2019), enabling the circulation of fluids. Scoria (or pumice in dacitic to rhyolitic environments) fragments large

enough to core and study mechanically are rare. Additionally, many pyroclastic rocks are too soft or incoherent to be cored. Thus, this study, like many others, was limited in pyroclastic sampling, which limits our ability to derive patterns in their physical and mechanical properties.

Fresh rock tends to be less porous and stronger than rock with surface weathering, which is less porous and weaker than rock with supergene or steam-heated advanced argillic weathering (Figure 6, Figure 10, Figure 4A, B). A larger percentage of weathering and alteration to clay minerals generally reduces strength and increases the propensity for ductile behavior (Figure 6D, Figure 10, Figure 4A-B, E-F; as also observed by Siratovich et al., 2016; Mordensky et al., 2019a), with the degree/intensity of clay alteration negatively correlating to UCS and Young's modulus (Figure 10G-J; as also observed by Watters et al., 2000). Alteration mineralogy is not a function of the primary lithology (Figure 6A and 6B), but rather of the local hydrothermal history of the volcano. Thus, there are limitations to assuming that all steam-heated rocks will be weaker than all fresh rocks, as primary porosity and rock history needs to be taken into consideration. In our dataset, this is clear in the strong scatter within the minor and moderate alteration pervasiveness categories, and in surface weathering and supergene weathering categories (Figure 10).

Some characteristics, such as UCS, static Young's modulus, and $m_i$, systematically vary with increasing alteration style and pervasiveness, allowing for a clear distinction between fresh and altered rock (Figure 10G-L), as also shown in (Heap et al., 2021). Porosity, permeability, and Vp have larger data spreads in weathered and altered rock than in fresh rock (Figure 10A-F), which also reduces systematic trends through alteration type and pervasiveness. Porosity tends to increase with increasing alteration type and pervasiveness, however this porosity relationship does not apply to steam-heated and pervasively altered samples (Figure 10A, B). This could be a function of the small sample number, which in turn is a function of the difficulty of sampling these rock types.

Permeability remains within one order of magnitude for all alteration types and pervasiveness, except for supergene and moderate alteration (Figure 10C, D). Supergene and moderate alteration appear to have a wide range of effects on permeability, although the reason for this is not yet clear due to a small sample number. Additional steam-heated or pervasively altered samples would further clarify the trends seen in this dataset. Pervasively altered samples tend to have the lowest Vp, although a systematic trend through alteration pervasiveness (as observed by other authors e.g., Pola et al., 2012) is less obvious (Figure 10E, F).

The effects of rock physical and mechanical properties vary depending on the rock characteristics; for example, porosity may be a better predictor of UCS than alteration type or pervasiveness for rocks with porosity >10%, whereas alteration and pervasiveness may be better predictors for lavas (which tend to have lower porosity). These trends are affected by high-intensity hydrothermal alteration (e.g., Heap et al., 2019b), which develops when rocks are in close proximity to an active hydrothermal system or are exposed to hydrothermal fluid circulation for long periods. This can lead to both mineral replacement (primary minerals to clay) and precipitation of clay into pores and cracks, resulting in anomalously low porosity, low strength samples (e.g., Siratovich et al., 2014; Wyering et al., 2014). This is highlighted by samples RH50 and RH52 (Figure 6). Sample RH52 is a block of lava taken from the edge of the Crater Lake. The Crater Lake is highly acidic (pH = 0-3) and fluctuates in temperatures (e.g., 20-45°C), therefore this sample was subjected to intense alteration and precipitation of clay infilling minerals, particularly in the outer 6 cm, resulting in lower porosity to UCS ratios than is typical for lava with low primary porosity (Figure 6). Sample RH50, a block from the 1995-1996 eruption, represents lava from the upper conduit area within the current vent hosted hydrothermal system (Kilgour et

al., 2010). RH50 has a high percentage of altered clay, resulting in anomalously low porosity, low strength, and low magnetic susceptibility. This points to complex relationships between porosity, mineralogy and physical and mechanical characteristics that remain to be thoroughly explored.

An additional consideration for material property variations is alteration rate, and spatial and temporal position to aggressive fluids. Alteration by acidic fluids is fairly rapid ((Farquharson et al., 2019), and likely faster than surface weathering processes. For example, samples RH52 and RH42B were both formed in the youngest Whakapapa formation (≤15 ky), however RH52 was directly exposed to acidic Crater Lake fluids and has moderate alteration despite having very low porosity, while RH42B was not exposed to acidic fluids and remains a fresh sample despite being one of the highest porosity samples. Samples RH28 and RH22 are both part of the Te Herenga formation (200 to 150 ka), but RH28 was altered via hydrothermal alteration while RH22 was altered via surface weathering. Thus, RH28 is more pervasively altered and contains more clay and sulphide minerals than RH22. However, the very long exposure time of RH22 to weathering has resulted in anomalously high permeability for the given porosity, and a low Young's modulus (Figure 7).

### *4.3 Implications for monitoring, modeling, and volcanic hazards*

Sample RH50, a lava rock which originated from the upper conduit and was brought to the surface during the 1995-1996 eruptions, highlights that surface characteristics cannot always be used to infer subsurface properties, especially with respect to hydrothermal alteration. The low strength of RH50 due to the high percentage of clay minerals suggests that material in the upper conduit area of Mt Ruapehu could be two times weaker than typical porosity-strength trends of surface samples; RH50 has an average UCS of 93 MPa (Table 3) while the exponential trend suggests a rock with a porosity c. 3.6% would have a UCS c. 190 MPa (Figure 6). This has significant implications for stability modeling. Low apparent magnetic susceptibility (<0.005 SI), interpreted as a region of altered rock in the current hydrothermal system, has been mapped beneath the Crater Lake extending to ~1700 m a.s.l. using an aeromagnetic data inversion (Miller et al., 2020). Other low susceptibility areas have been mapped within the upper cone flanks using a combination of aeromagnetic and hyperspectral surveys, and interpreted to be part of older hydrothermal systems (Kereszturi et al., 2020). Thus, larger areas of weak, soft, and altered material may be present throughout Mt. Ruapehu's upper flanks than previously expected, or that is obvious from surface observations. This emphasizes the benefit of using ballistics (fragments of rock expelled during explosive eruptions, such as block RH50) that have originated from the subsurface to measure the properties in currently active hydrothermal systems (Kennedy et al., 2020). However, subsurface samples useful for mechanical testing are rare, and those that are acquired may require assumptions regarding sample origin and environment. Thus, determining subsurface material properties, especially at meaningful resolution and under realistic laboratory conditions (e.g.,, varying confining pressures, temperatures, and saturation), remains a challenge.

This dataset additionally emphasizes that although trends of weathering/alteration and material properties do exist, properties of volcanic rock can vary significantly within each category and within hand-specimen scales. However, fresh material is typically distinguishable from moderately or pervasively altered rock, which suggests that end member differentiation is possible for physical and mechanical property mapping. The generally strong control of porosity on other physical and mechanical properties suggests that more accurate relations can be made if a dataset is split into porosity groups; this is apparent when we split samples by lithology (Figure 7), which typically have distinct porosities due to emplacement mechanisms. This will likely result in

physical and mechanical input data at higher spatial resolution than is typically used in geophysical models (e.g., Heap et al., 2020).

### *4.4. Implications for spectroscopy-material property correlations*

Our data show that as alteration becomes more prominent, there is a spectral shift from 540 nm to <450 nm, indicating the occurrence of goethite (430 and 480 nm; Figure 3A) as a weathering product of hydrothermal pyrite (Kereszturi et al., 2020), and precipitation of native sulfur (390 nm; Figure 3A). This alteration-induced shift in wavelength location (Figure 3A) also coincides with alteration-induced changes to material properties (Figure 10). Using Spearman's ρ statistical value, Schaefer et al. (2021) demonstrate that these tandem shifts result in strong correlations between laboratory reflectance values and rock properties such as magnetic susceptibility, UCS, porosity, density, friction angle, and static Young's modulus. The laboratory spectral signatures of carbonate rocks have also recently been shown to correlate with rock strength (Bakun-Mazor et al., 2021). Given the resource- and time-consuming efforts required to characterize rocks in a laboratory setting, future efforts could explore direct correlations of spectroscopy with physical and mechanical rock properties. Remotely-sensed spectroscopy at volcanoes (e.g., Aslett et al., 2018; Kereszturi et al., 2018; Gabrieli et al., 2019) can further support the spatial interpolation of sparsely sampled material data, resulting in large-scale geotechnical maps.

## 5. Conclusion

Physical and mechanical properties were determined for a suite of 23 blocks of andesitic lavas, autoclastic breccias, and pyroclastic rocks from Mt. Ruapehu volcano in New Zealand with varying weathering and alteration mineralogies and intensities. The large number of samples of lavas and autoclastic breccias allowed the distinction of material relations and systemic changes due to weathering and alteration heterogeneities for these rock types. Expanding this research to include volcanic material from other locations (surface and subsurface) will continue to develop these relationships. Our key findings are:

(1) Porosity has a dominant effect on many physical and mechanical properties. Lavas typically having lower porosities (< 20%) than autoclastic breccias (> 20 %) or tephra (> 40%).

(2) Weathering and alteration, including both the type of alteration and alteration intensity, additionally influence physical and mechanical rock properties. Uniaxial compressive strength, static Young's modulus, and Hoek-brown constant $m_i$ were found to have more systematic variations with weathering/alteration mineralogy and pervasiveness than variables such as permeability and seismic velocities.

(3) Fresh rock tends to be less porous and stronger than rock with surface weathering. Rock with surface weathering is less porous, stronger, and behaves less brittle than rock with supergene or steam-heated intermediate and advanced argillic weathering.

(4) In addition to porosity and strength, P-wave velocity, density, and Young's modulus show strong relationships with other material properties.

(5) End-member property differentiation is easily distinguishable (e.g., fresh vs. pervasively altered rock). However, rocks with minor to intermediate weathering or alteration tend to have larger variations in properties due to varying consequences of the nature of the host rock, the fluid type and composition, temperature, and the duration of rock-fluid interaction.

(6) Samples near the active hydrothermal system do not follow typical porosity-strength trends as surface samples due to the intensity of clay mineral precipitation and replacement. This has implications for varying the brittle-ductile transition zone, preventing fluid flow, and increasing the likelihood of collapse.
(7) Trends in the pervasiveness of weathering and alteration suggest the possibility of correlating physical and mechanical intact rock properties to laboratory or imaging spectroscopy measurements.


## 6. Acknowledgements

The Authors are grateful for Department of Conservation and Iwi around the Tongariro National Park for providing sampling permits (Authorization Number: 63618-GEO), and to all student and staff who joined in fieldwork and sampling campaigns throughout this project.


## 7. Declarations


*7.1. Funding*

This research was supported by the New Zealand Ministry of Business, Innovation & Employment's Natural Hazards Research Platform for the project "Too big to fail? – A multidisciplinary approach to predict collapse and debris flow hazards from Mt. Ruapehu".


*7.2. Conflicts of interest*

The authors have no conflicts of interest to declare that are relevant to the content of this article.

*7.3. Data availability*

Physical and mechanical results for each specimen, and calculated strength criteria for each block using the Mohr-Coulomb and Generalized Hoek-Brown methods, are available in the Supplementary Material. Additional data are available from the corresponding author upon request.

## 8. References


Al-Harthi, A.A., Al-Amri, R.M., and Shehata, W.M., 1999, The porosity and engineering properties of vesicular basalt in Saudi Arabia: Engineering Geology, doi:10.1016/S0013-7952(99)00050-2.

Apuani, T., Corazzato, C., Cancelli, A., and Tibaldi, A., 2005, Stability of a collapsing volcano (Stromboli, Italy): Limit equilibrium analysis and numerical modelling: Journal of Volcanology and Geothermal Research, v. 144, p. 191–210.

Aslett, Z., Taranik, J. V., and Riley, D.N., 2018, Mapping rock forming minerals at Boundary Canyon, Death Valey National Park, California, using aerial SEBASS thermal infrared hyperspectral image data: International Journal of Applied Earth Observation and Geoinformation, doi:10.1016/j.jag.2017.08.001.

Bakun-Mazor, D., Ben-Ari, Y., Notesko, G., Marco, S., and Ben-Dor, E., 2021, Measuring Carbonate Rock Strength using Spectroscopy across the Optical and Thermal Region, *in* IOP Conference Series: Earth and Environmental Science, IOP Publishing, v. 833, p. 012025.

Ball, J.L., Calder, E.S., Hubbard, B.E., and Bernstein, M.L., 2013, An assessment of hydrothermal alteration in the Santiaguito lava dome complex, Guatemala: Implications for dome collapse hazards: Bulletin of Volcanology, doi:10.1007/s00445-012-0676-z.

673 Ball, J.L., Taron, J., Reid, M.E., Hurwitz, S., Finn, C., and Bedrosian, P., 2018, Combining
674 Multiphase Groundwater Flow and Slope Stability Models to Assess Stratovolcano Flank
675 Collapse in the Cascade Range: Journal of Geophysical Research: Solid Earth,
676 doi:10.1002/2017JB015156.
677 Brace, W.F., Walsh, J.B., and Frangos, W.T., 1968, Permeability of granite under high pressure:
678 Journal of Geophysical Research, doi:10.1029/jb073i006p02225.
679 Cai, M., 2010, Practical estimates of tensile strength and Hoek-Brown strength parameter mi of
680 brittle rocks: Rock Mechanics and Rock Engineering, doi:10.1007/s00603-009-0053-1.
681 Cant, J.L., Siratovich, P.A., Cole, J.W., Villeneuve, M.C., and Kennedy, B.M., 2018, Matrix
682 permeability of reservoir rocks, Ngatamariki geothermal field, Taupo Volcanic Zone,
683 New Zealand: Geothermal Energy, doi:10.1186/s40517-017-0088-6.
684 Carter, T., 2020, A suggested visual approach for estimating Hoek-Brown mi for different rock
685 types, In Conference: ISRM Congress: Rock Mechanics for Natural Resources and
686 Infrastructure Development, Foz do Iguassu, Brazil, ISBN: 978-0-367-42284-4.
687 Christenson, B.W., 2000, Geochemistry of fluids associated with the 1995-1996 eruption of Mt.
688 Ruapehu, New Zealand: Signatures and processes in the magmatic-hydrothermal system,
689 *in* Journal of Volcanology and Geothermal Research, doi:10.1016/S0377-
690 0273(99)00167-5.
691 Christenson, B.W., and Wood, C.P., 1993, Evolution of a vent-hosted hydrothermal system
692 beneath Ruapehu Crater Lake, New Zealand: Bulletin of volcanology, v. 55, p. 547–565,
693 doi:10.1007/BF00301808.
694 Clarke, R., 1999, Chapter 1: Spectroscopy of rocks and minerals, and principles of spectroscopy,
695 Manual of Remote Sensing: Remote Sensing for the Earth Sciences, p. 3–58.
696 Coats, R., Kendrick, J.E., Wallace, P.A., Miwa, T., Hornby, A.J., Ashworth, J.D., Matsushima,
697 T., and Lavallée, Y., 2018, Failure criteria for porous dome rocks and lavas: a study of
698 Mt. Unzen, Japan: Solid Earth, v. 9, p. 1299–1328, doi:doi.org/10.5281/zenodo.1287237.
699 Conway, C.E., Leonard, G.S., Townsend, D.B., Calvert, A.T., Wilson, C.J.N., Gamble, J.A., and
700 Eaves, S.R., 2016, A high-resolution 40Ar/39Ar lava chronology and edifice construction
701 history for Ruapehu volcano, New Zealand: Journal of Volcanology and Geothermal
702 Research, doi:10.1016/j.jvolgeores.2016.07.006.
703 Crowley, J.K., and Zimbelman, D.R., 1997, Mapping hydrothermally altered rocks on Mount
704 Rainier, Washington, with Airborne Visible/Infrared Imaging Spectrometer (AVIRIS)
705 data: Geology, doi:10.1130/0091-7613(1997)025<0559:MHAROM>2.3.CO;2.
706 Danner, M., Locherer, M., Hank, T., Richter, K., and others, 2015, Spectral Sampling with the
707 ASD FIELDSPEC 4:
708 Day, S.J., 1996, Hydrothermal pore fluid pressure and the stability of porous, permeable
709 volcanoes: Geological Society, London, Special Publications, v. 110, p. 77–93,
710 doi:10.1144/GSL.SP.1996.110.01.06.
711 Dobson, P.F., Kneafsey, T.J., Hulen, J., and Simmons, A., 2003, Porosity, permeability, and fluid
712 flow in the Yellowstone geothermal system, Wyoming: Journal of Volcanology and
713 Geothermal Research, doi:10.1016/S0377-0273(03)00039-8.
714 Farquharson, J.I., Wild, B., Kushnir, A.R.L., Heap, M.J., Baud, P., and Kennedy, B., 2019, Acid-
715 Induced Dissolution of Andesite: Evolution of Permeability and Strength: Journal of
716 Geophysical Research: Solid Earth, doi:10.1029/2018JB016130.
717 Frolova, J. V, Gvozdeva, I.P., and Kuznetsov, N.P., 2015, Effects of Hydrothermal Alterations
718 on Physical and Mechanical Properties of Rocks in the Geysers Valley (Kamchatka

719 Peninsula) in Connection with Landslide Development: World Geotermal Congress
720 2015,.
721 Gabrieli, A., Wright, R., Porter, J.N., Lucey, P.G., and Honnibal, C., 2019, Applications of
722 quantitative thermal infrared hyperspectral imaging (8–14 μm): measuring volcanic SO2
723 mass flux and determining plume transport velocity using a single sensor: Bulletin of
724 Volcanology, doi:10.1007/s00445-019-1305-x.
725 Gonnermann, H.M., and Manga, M., 2007, The Fluid Mechanics Inside a Volcano: Annual
726 Review of Fluid Mechanics, doi:10.1146/annurev.fluid.39.050905.110207.
727 Guéguen, Y., and Palciauskas, V., 1994, Introduction to the Physics of Rocks: Princeton
728 University Press.
729 Hackett, W.R., 1985, Geology and petrology of Ruapehu volcano and related vents: PhD
730 dissertation,.
731 Hackett, W.R., and Houghton, B.F., 1989, A facies model for a quaternary andesitic composite
732 volcano: Ruapehu, New Zealand: Bulletin of Volcanology, doi:10.1007/BF01086761.
733 Heald, P., Foley, N.K., and Hayba, D.O., 1987, Comparative anatomy of volcanic-hosted
734 epithermal deposits: acid- sulfate and adularia- sericite types.: Economic Geology,
735 doi:10.2113/gsecongeo.82.1.1.
736 Heap, M.J. et al., 2021, Alteration-Induced Volcano Instability at La Soufrière de Guadeloupe
737 (Eastern Caribbean): Journal of Geophysical Research: Solid Earth, v. 126, p.
738 e2021JB022514.
739 Heap, M.J., Farquharson, J.I., Baud, P., Lavallée, Y., and Reuschlé, T., 2015a, Fracture and
740 compaction of andesite in a volcanic edifice: Bulletin of Volcanology,
741 doi:10.1007/s00445-015-0938-7.
742 Heap, M.J., Farquharson, J.I., Wadsworth, F.B., Kolzenburg, S., and Russell, J.K., 2015b,
743 Timescales for permeability reduction and strength recovery in densifying magma: Earth
744 and Planetary Science Letters, doi:10.1016/j.epsl.2015.07.053.
745 Heap, M.J., Gravley, D.M., Kennedy, B.M., Gilg, H.A., Bertolett, E., and Barker, S.L.L., 2019a,
746 Quantifying the role of hydrothermal alteration in creating geothermal and epithermal
747 mineral resources: The Ohakuri ignimbrite (Taupo Volcanic Zone, New Zealand):
748 Journal of Volcanology and Geothermal Research, p. 106703,
749 doi:10.1016/j.jvolgeores.2019.106703.
750 Heap, M.J., Kennedy, B.M., Pernin, N., Jacquemard, L., Baud, P., Farquharson, J.I., Scheu, B.,
751 Lavallée, Y., Gilg, H.A., and Letham-Brake, M., 2015c, Mechanical behaviour and
752 failure modes in the Whakaari (White Island volcano) hydrothermal system, New
753 Zealand: Journal of Volcanology and Geothermal Research, v. 295, p. 26–42,
754 doi:10.1016/j.jvolgeores.2015.02.012.
755 Heap, M.J., Lavallée, Y., Petrakova, L., Baud, P., Reuschle, T., Varley, N.R., and Dingwell,
756 D.B., 2014a, Microstructural controls on the physical and mechanical properties of
757 edifice-forming andesites at Volcán de Colima, Mexico: Journal of Geophysical
758 Research: Solid Earth, v. 119, p. 2925–2963, doi:10.1002/2013JB010521.
759 Heap, M.J., Troll, V.R., Kushnir, A.R.L., Gilg, H.A., Collinson, A.S.D., Deegan, F.M.,
760 Darmawan, H., Seraphine, N., Neuberg, J., and Walter, T.R., 2019b, Hydrothermal
761 alteration of andesitic lava domes can lead to explosive volcanic behaviour: Nature
762 Communications, doi:10.1038/s41467-019-13102-8.
763 Heap, M.J., Villeneuve, M., Albino, F., Farquharson, J.I., Brothelande, E., Amelung, F., Got,
764 J.L., and Baud, P., 2020, Towards more realistic values of elastic moduli for volcano

765 modelling: Journal of Volcanology and Geothermal Research,
766 doi:10.1016/j.jvolgeores.2019.106684.
767 Heap, M.J., Xu, T., and Chen, C. feng, 2014b, The influence of porosity and vesicle size on the
768 brittle strength of volcanic rocks and magma: Bulletin of Volcanology,
769 doi:10.1007/s00445-014-0856-0.
770 Hickey, J., Lloyd, R., Biggs, J., Arnold, D., Mothes, P., and Muller, C., 2020, Rapid localized
771 flank inflation and implications for potential slope instability at Tungurahua volcano,
772 Ecuador: Earth and Planetary Science Letters, doi:10.1016/j.epsl.2020.116104.
773 Hill, S., 2020, Mechanical rock property characterisation and assessment of sandstone reservoirs
774 in the Southern Taranaki Basin: PhD Thesis, University of Canterbury.
775 Huang, Z., Turner, B.J., Dury, S.J., Wallis, I.R., and Foley, W.J., 2004, Estimating foliage
776 nitrogen concentration from HYMAP data using continuum removal analysis: Remote
777 Sensing of Environment, v. 93, p. 18–29.
778 Hunt, G.R., and Ashley, R.P., 1979, Spectra of altered rocks in the visible and near infrared:
779 Economic Geology, doi:10.2113/gsecongeo.74.7.1613.
780 Kennedy, B.M., Farquhar, A., Hilderman, R., Villeneuve, M.C., Heap, M.J., Mordensky, S.,
781 Kilgour, G., Jolly, A., Christenson, B., and Reuschlé, T., 2020, Pressure controlled
782 permeability in a conduit filled with fractured hydrothermal Breccia reconstructed from
783 ballistics from Whakaari (White island), New Zealand: Geosciences,
784 doi:10.3390/geosciences10040138.
785 Kereszturi, G., Schaefer, L.N., Miller, C., and Mead, S., 2020, Hydrothermal Alteration on
786 Composite Volcanoes -Mineralogy, Hyperspectral Imaging and Aeromagnetic Study of
787 Mt Ruapehu, New Zealand: Geochemistry, Geophysics, Geosystems,
788 doi:https://doi.org/10.1029/2020GC009270.
789 Kereszturi, G., Schaefer, L.N., Schleiffarth, W.K., Procter, J., Pullanagari, R.R., Mead, S., and
790 Kennedy, B., 2018, Integrating airborne hyperspectral imagery and LiDAR for volcano
791 mapping and monitoring through image classification: International Journal of Applied
792 Earth Observation and Geoinformation, doi:10.1016/j.jag.2018.07.006.
793 Kilgour, G., V. Manville, Pasqua, F. Della, A. Graettinger, Hodgson, K.A., and Jolly, G.E.,
794 2010, The 25 September 2007 eruption of Mount Ruapehu, New Zealand: Directed
795 ballistics, surtseyan jets, and ice-slurry lahars: Journal of Volcanology and Geothermal
796 Research, doi:10.1016/j.jvolgeores.2009.10.015.
797 Kokaly, R.F., and Clark, R.N., 1999, Spectroscopic determination of leaf biochemistry using
798 band-depth analysis of absorption features and stepwise multiple linear regression:
799 Remote sensing of environment, v. 67, p. 267–287.
800 Labuz, J.F., and Zang, A., 2012, Mohr–Coulomb failure criterion, *in* The ISRM Suggested
801 Methods for Rock Characterization, Testing and Monitoring: 2007-2014, Springer, p.
802 227–231.
803 Laukamp, C., Rodger, A., LeGras, M., Lampinen, H., Lau, I.C., Pejcic, B., Stromberg, J.,
804 Francis, N., and Ramanaidou, E., 2021, Mineral Physicochemistry Underlying Feature-
805 Based Extraction of Mineral Abundance and Composition from Shortwave, Mid and
806 Thermal Infrared Reflectance Spectra: Minerals, v. 11, doi:10.3390/min11040347.
807 López, D.L., and Williams, S.N., 1993, Catastrophic volcanic collapse: Relation to hydrothermal
808 processes: Science, doi:10.1126/science.260.5115.1794.
809 Lu, Z., Masterlark, T., and Dzurisin, D., 2005, Interferometric synthetic aperture radar study of
810 Okmok volcano, Alaska, 1992–2003: Magma supply dynamics and postemplacement

lava flow deformation: Journal of Geophysical Research: Solid Earth (1978–2012), v. 110, doi:10.1029/2004JB003148.
van der Meer, F., 2018, Near-infrared laboratory spectroscopy of mineral chemistry: A review: International Journal of Applied Earth Observation and Geoinformation, doi:10.1016/j.jag.2017.10.004.
Miller, C., Schaefer, L.N., Kereszturi, G., and Fournier, D., 2020, Three dimensional mapping of Mt Ruapehu volcano, New Zealand, from aeromagnetic data inversion and hyperspectral imaging.: Journal of Geophysical Research: Solid Earth, v. 125, doi:10.1029/2019JB018247.
Mordensky, S.P., Heap, M.J., Kennedy, B.M., Gilg, H.A., Villeneuve, M.C., Farquharson, J.I., and Gravley, D.M., 2019a, Influence of alteration on the mechanical behaviour and failure mode of andesite: implications for shallow seismicity and volcano monitoring: Bulletin of Volcanology, doi:10.1007/s00445-019-1306-9.
Mordensky, S.P., Kennedy, B.M., Villeneuve, M.C., Lavallée, Y., Reichow, M.K., Wallace, P.A., Siratovich, P.A., and Gravley, D.M., 2019b, Increasing the Permeability of Hydrothermally Altered Andesite by Transitory Heating: Geochemistry, Geophysics, Geosystems, doi:10.1029/2019GC008409.
Mordensky, S.P., Villeneuve, M.C., Kennedy, B.M., Heap, M.J., Gravley, D.M., Farquharson, J.I., and Reuschlé, T., 2018, Physical and mechanical property relationships of a shallow intrusion and volcanic host rock, Pinnacle Ridge, Mt. Ruapehu, New Zealand: Journal of Volcanology and Geothermal Research, doi:10.1016/j.jvolgeores.2018.05.020.
Nakagawa, M., Wada, K., Thordarson, T., Wood, C.P., and Gamble, J.A., 1999, Petrologic investigations of the 1995 and 1996 eruptions of Ruapehu volcano, New Zealand: Formation of discrete and small magma pockets and their intermittent discharge: Bulletin of Volcanology, doi:10.1007/s004450050259.
Neal, L.C., Wilkinson, J.J., Mason, P.J., and Chang, Z., 2018, Spectral characteristics of propylitic alteration minerals as a vectoring tool for porphyry copper deposits: Journal of Geochemical Exploration, doi:10.1016/j.gexplo.2017.10.019.
Okada, N., Maekawa, Y., Owada, N., Haga, K., Shibayama, A., and Kawamura, Y., 2020, Automated Identification of Mineral Types and Grain Size Using Hyperspectral Imaging and Deep Learning for Mineral Processing: Minerals, v. 10, doi:10.3390/min10090809.
Pola, A., Crosta, G., Fusi, N., Barberini, V., and Norini, G., 2012, Influence of alteration on physical properties of volcanic rocks: Tectonophysics, doi:10.1016/j.tecto.2012.07.017.
Price, R.C., Gamble, J.A., Smith, I.E.,M., Maas, R., Waight, T., Stewart, R.B., and Woodhead, J., 2012, The anatomy of an andesite volcano: A time-stratigraphic study of andesite petrogenesis and crustal evolution at Ruapehu Volcano, New Zealand: Journal of Petrology, doi:10.1093/petrology/egs050.
Reid, M.E., Sisson, T.W., and Brien, D.L., 2001, Volcano collapse promoted by hydrothermal alteration and edifice shape, Mount Rainier, Washington: Geology, v. 29, p. 779–782, doi:10.1130/0091-7613(2001)029<0779:VCPBHA>2.0.CO;2.
Richards, L.R., and Read, S.A.L., 2011, A comparison of methods for determining mi, the Hoek-Brown parameter for intact rock material: 45th US Rock Mechanics / Geomechanics Symposium,.
Ruitenbeek, F.J.A. van, Werff, H.M.A. van der, Bakker, W.H., Meer, F.D. van der, and Hein, K.A.A., 2019, Measuring rock microstructure in hyperspectral mineral maps: Remote Sensing of Environment, v. 220, p. 94–109, doi:https://doi.org/10.1016/j.rse.2018.10.030.

Rye, R.O., 2005, A review of the stable-isotope geochemistry of sulfate minerals in selected igneous environments and related hydrothermal systems: Chemical Geology, doi:10.1016/j.chemgeo.2004.06.034.

Saubin, E., Kennedy, B., Tuffen, H., Villeneuve, M., Davidson, J., and Burchardt, S., 2019, Comparative field study of shallow rhyolite intrusions in Iceland: Emplacement mechanisms and impact on country rocks: Journal of Volcanology and Geothermal Research, doi:10.1016/j.jvolgeores.2019.106691.

Schaefer, L.N., Kendrick, J.E., Lavallée, Y., Oommen, T., and Chigna, G., 2015, Geomechanical rock properties of a basaltic volcano: Frontiers in Earth Science, v. 3, p. 29, doi:10.3389/feart.2015.00029.

Schaefer, L.N., Kereszturi, G., Villeneuve, M., and Kennedy, B., 2021, Determining physical and mechanical volcanic rock properties via reflectance spectroscopy: Journal of Volcanology and Geothermal Research, v. 420, p. 107393, doi:https://doi.org/10.1016/j.jvolgeores.2021.107393.

Schaefer, L.N., Oommen, T., Corazzato, C., Tibaldi, A., Escobar-Wolf, R., and Rose, W.I., 2013, An integrated field-numerical approach to assess slope stability hazards at volcanoes: the example of Pacaya, Guatemala: Bulletin of volcanology, v. 75, p. 1–18, doi:10.1007/s00445-013-0720-7.

Schwertmann, U., and Murad, E., 1983, Effect of pH on the formation of goethite and hematite from ferrihydrite.: Clays & Clay Minerals, doi:10.1346/CCMN.1983.0310405.

Scott, B.J., 2013, A revised catalogue of Ruapehu volcano eruptive activity: 1830-2012: GNS Science Open Report.

Severin, K.P., 2004, Energy dispersive spectrometry of common rock forming minerals: Springer.

Shindo, D., and Oikawa, T., 2002, Energy dispersive x-ray spectroscopy, *in* Analytical electron microscopy for materials science, Springer, p. 81–102.

Simmons, S.F., White, N.C., and John, D. a, 2005, Geological characteristics of epithermal precious and base metal deposits: Economic Geology; one hundredth anniversary volume, 1905-2005,.

Siratovich, P.A., Heap, M.J., Villeneuve, M.C., Cole, J.W., Kennedy, B.M., Davidson, J., and Reuschlé, T., 2016, Mechanical behaviour of the Rotokawa Andesites (New Zealand): Insight into permeability evolution and stress-induced behaviour in an actively utilised geothermal reservoir: Geothermics, doi:10.1016/j.geothermics.2016.05.005.

Siratovich, P.A., Heap, M.J., Villenueve, M.C., Cole, J.W., and Reuschlé, T., 2014, Physical property relationships of the Rotokawa Andesite, a significant geothermal reservoir rock in the Taupo Volcanic Zone, New Zealand: Geothermal Energy, doi:10.1186/s40517-014-0010-4.

Swayze, G.A. et al., 2014, Mapping advanced argillic alteration at Cuprite, Nevada, using imaging spectroscopy: Economic Geology, doi:10.2113/econgeo.109.5.1179.

Townsend, D., Leonard, G., Conway, C., Eaves, S., and Wilson, C., 2017, Geology of the Tongariro National Park Area 1:60 000: Lower Hutt, New Zealand, New Zealand, GNS Science.

Vanorio, T., Prasad, M., Patella, D., and Nur, A., 2002, Ultrasonic velocity measurements in volcanic rocks: Correlation with microtexture: Geophysical Journal International, doi:10.1046/j.0956-540x.2001.01580.x.

Villeneuve, M.C., and Heap, M.J., 2021, Calculating the cohesion and internal friction angle of volcanic rocks and rock masses: Volcanica, v. In press.
Villeneuve, M., Heap, M.J., and Schaefer, L.N., 2021, Defining the Hoek-Brown Constant mi for Volcanic Lithologies, *in* Fukuoka, Japan.
Villeneuve, M., Kennedy, B., Gravley, D., Mordensky, S.P., Heap, M.J., Siratovich, P., Wyering, L., and Cant, J., 2020, Characteristics of altered volcanic rocks in geothermal reservoirs, In Conference: ISRM Congress: Rock Mechanics for Natural Resources and Infrastructure Development, Foz do Iguassu, Brazil, ISBN: 978-0-367-42284-4:
Wallace, C.S., Schaefer, L.N., and Villeneuve, M.C., 2021, Material Properties and Triggering Mechanisms of an Andesitic Lava Dome Collapse at Shiveluch Volcano, Kamchatka, Russia, Revealed Using the Finite Element Method: Rock Mechanics and Rock Engineering, p. 1–18.
Watters, R.J., Zimbelman, D.R., Bowman, S.D., and Crowley, J.K., 2000, Rock mass strength assessment and significance to edifice stability, Mount Rainier and Mount Hood, Cascade Range volcanoes: Pure and Applied Geophysics, doi:10.1007/s000240050012.
Wong, T.F., and Baud, P., 2012, The brittle-ductile transition in porous rock: A review: Journal of Structural Geology, doi:10.1016/j.jsg.2012.07.010.
Wyering, L.D., Villeneuve, M.C., Wallis, I.C., Siratovich, P.A., Kennedy, B.M., Gravley, D.M., and Cant, J.L., 2014, Mechanical and physical properties of hydrothermally altered rocks, Taupo Volcanic Zone, New Zealand: Journal of Volcanology and Geothermal Research, v. 288, p. 76–93, doi:10.1016/j.jvolgeores.2014.10.008.
Yildiz, A., Kuşcu, M., Dumlupunar, I., Ekrem ArItan, A., and BağcI, M., 2010, The determination of the mineralogical alteration index and the investigation of the efficiency of the hydrothermal alteration on physico-mechanical properties in volcanic rocks from Köprülü, Afyonkarahisar, West Turkey: Bulletin of Engineering Geology and the Environment, doi:10.1007/s10064-009-0245-7.
Zimbelman, D.R., Rye, R.O., and Breit, G.N., 2005, Origin of secondary sulfate minerals on active andesitic stratovolcanoes: Chemical Geology, doi:10.1016/j.chemgeo.2004.06.056.

933 **Figures**

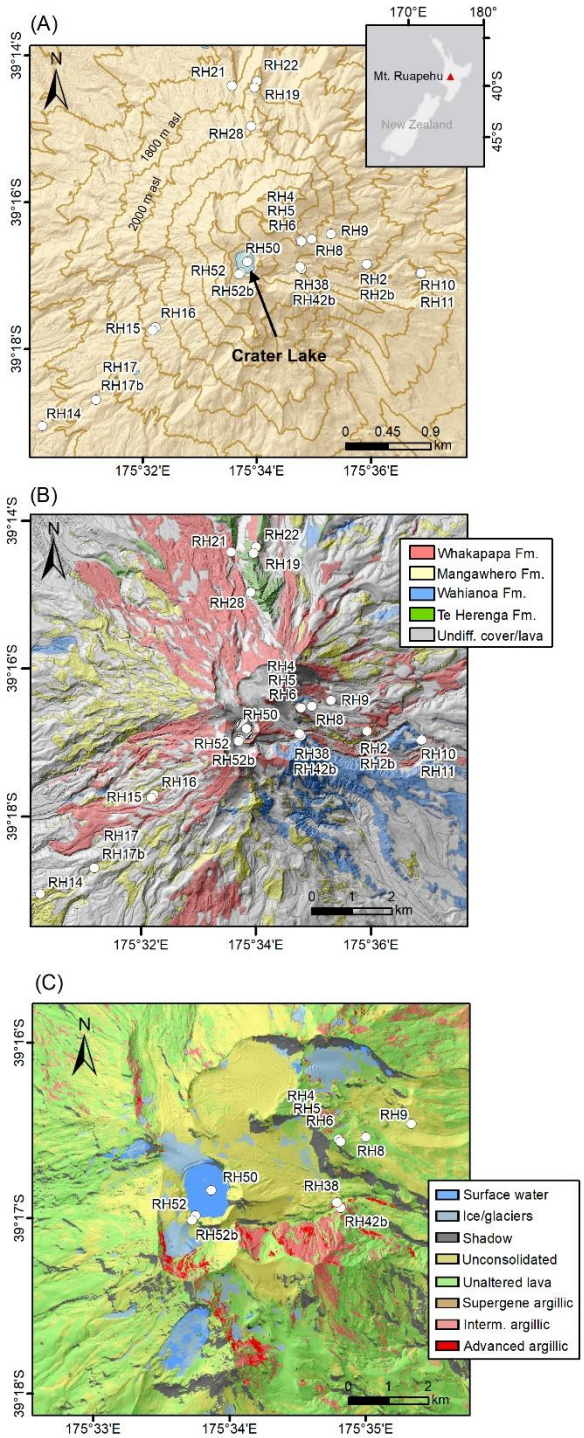


934
935 **Figure 1**. Location and variability of samples with respect to spectral properties and geological
936 formations. (A) Topographic map. (B) Alteration map based on airborne hyperspectral imagery
937 from Kereszturi et al. (2020b). (C) Simplified geological map, with the major geological
938 formations (after Townsend et al., 2017).
939

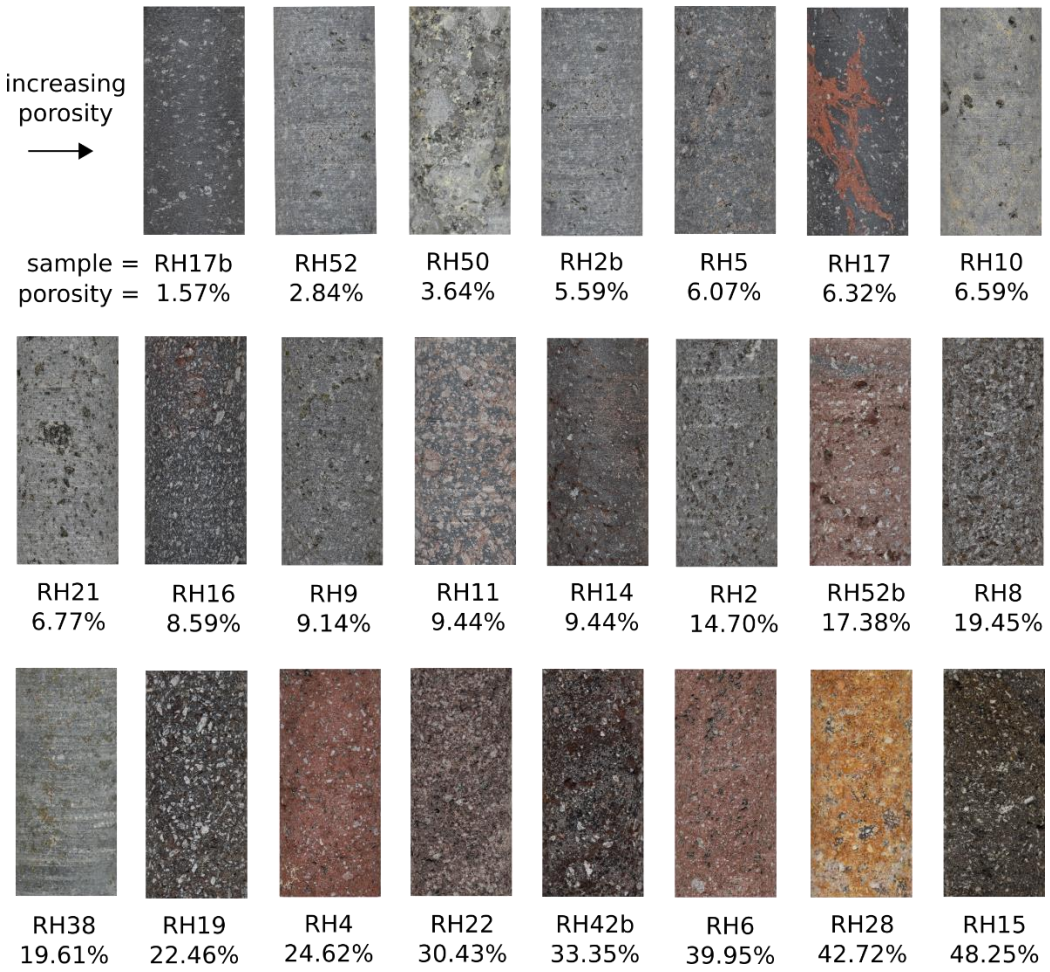


**Figure 2**. Photographs of the samples and porosity as determined by helium pycnometer.

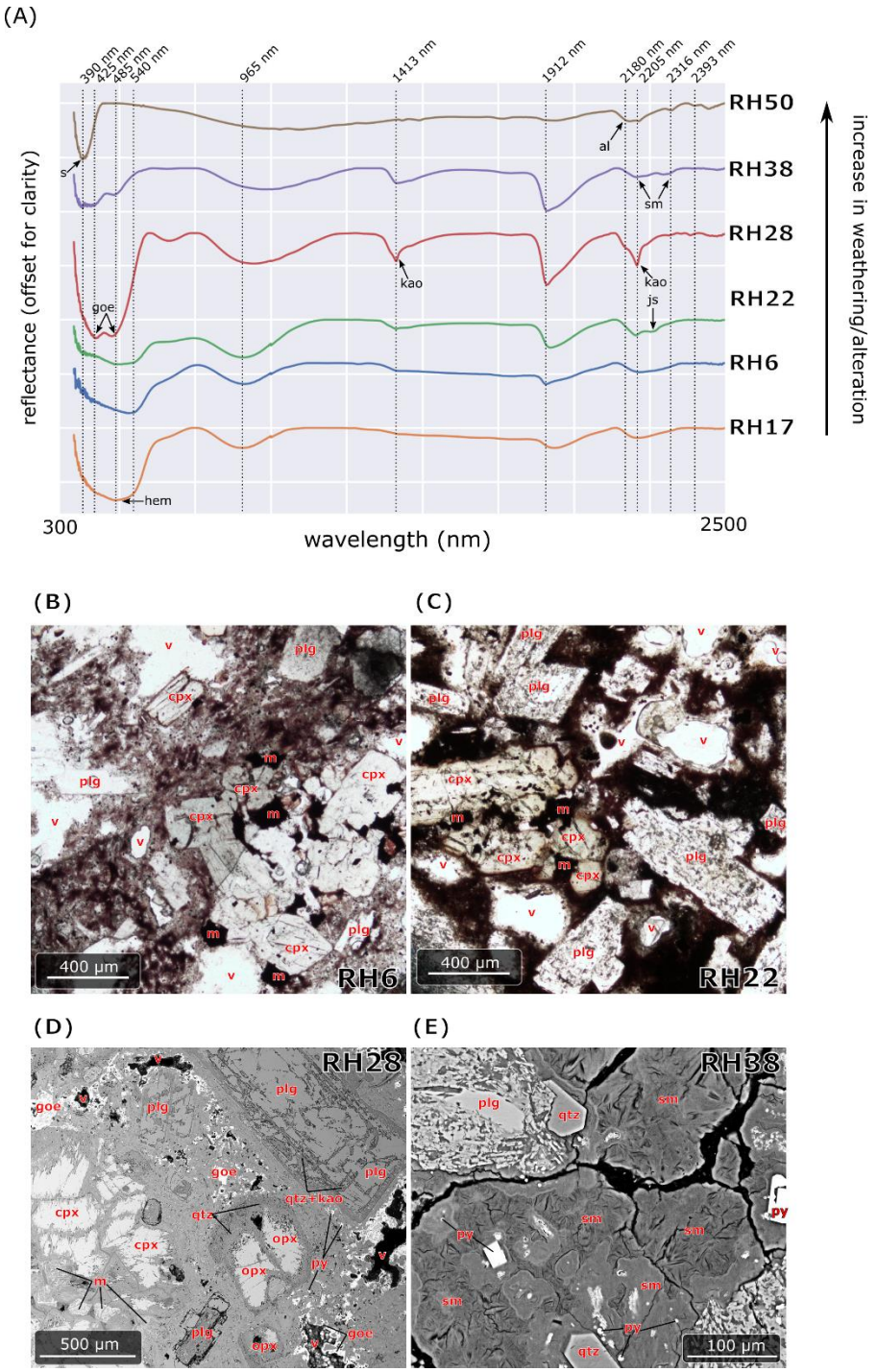


**Figure 3**. (A) Spectral reflectance curves of typical alteration minerals in volcanic environments from non-altered (RH17) to pervasively altered (RH50)- see descriptions in Table 3. Note the spectral shift from 550 nm to 480 nm where hematite is being replaced by goethite as a surface weathering product. (B-E) Optical microscope and SEM images demonstrating textural and mineralogical changes through hydrothermal and weathering alterations. Labeled mineral phases: v – void/vugg, m – titanomagnetite, plg – plagioclase, opx – orthopyroxene, cpx – clinopyroxene,

sm – smectites, kao – kaolinite, qtz – quartz, geo – goethite, py – pyrite, al – alunite, hem – hematite, s – sulfur.

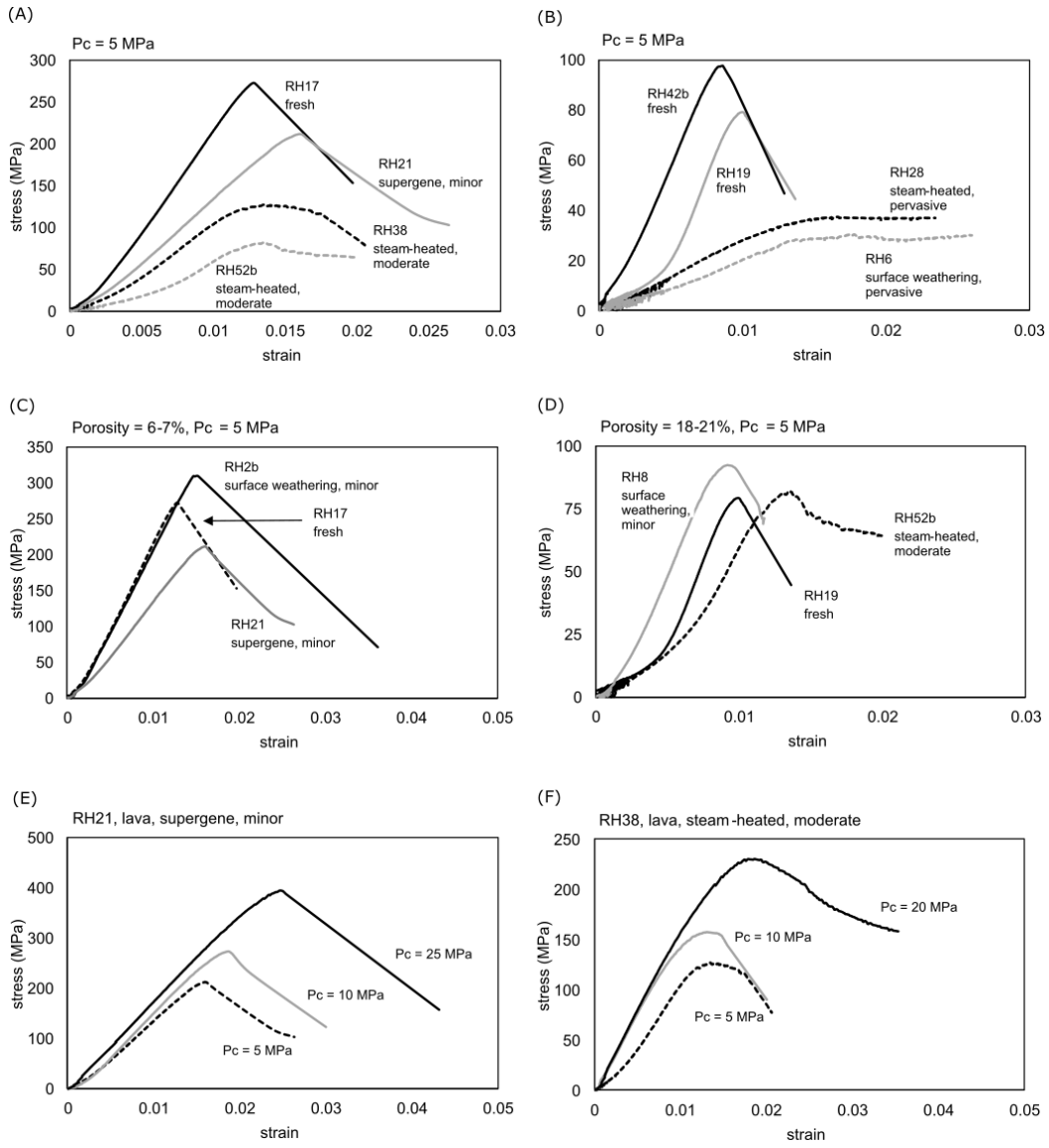


**Figure 4**. Stress-strain mechanical data from triaxial experiments. (A) Variably altered lava samples at a confining pressure (Pc) of 5 MPa (B) Variably altered autoclastic breccia samples also at Pc = 5 MPa. (C) Low porosity samples at Pc = 5 MPa (D) high porosity samples at Pc = 5 MPa. (E) Minor supergene and (F) moderate steam-heated lava sample behavior at three confining pressures.

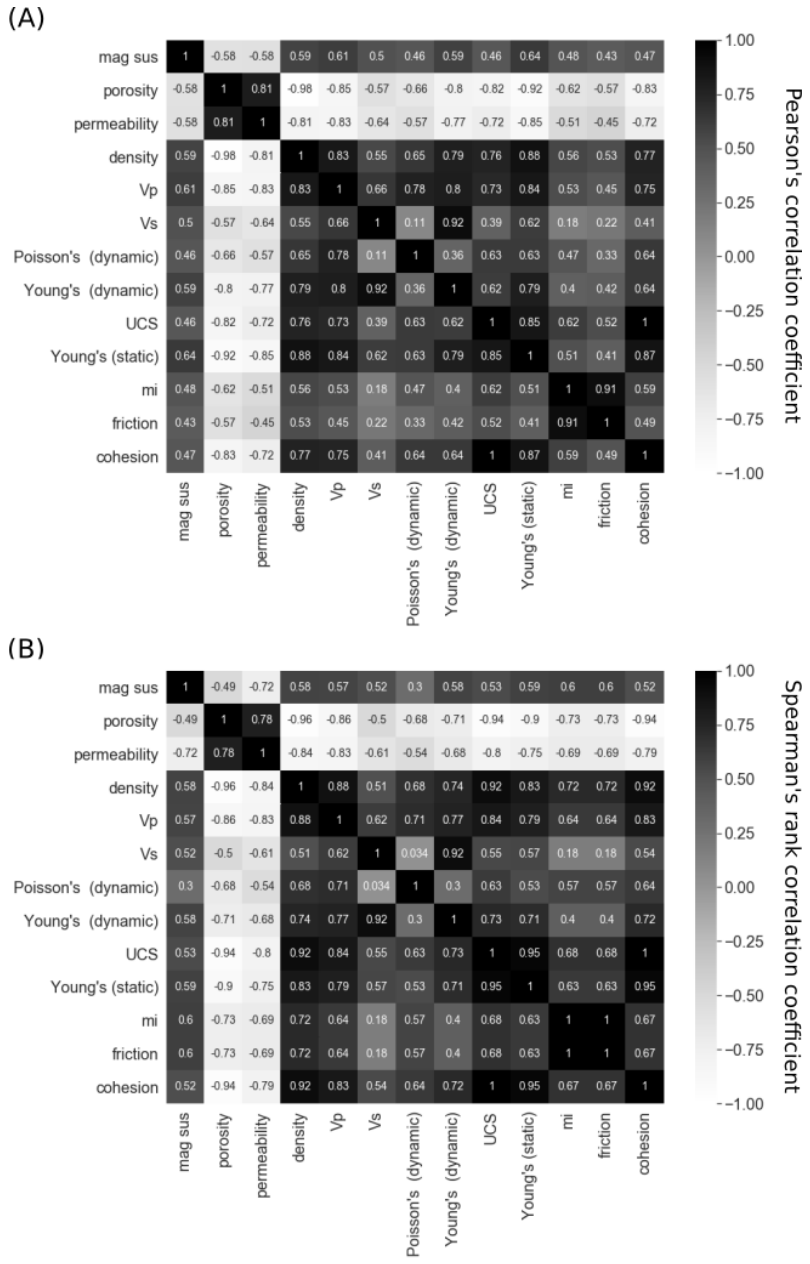


**Figure 5.** Correlation matrices between average block parameters, showing (A) linear (Pearson) and (B) monotonic (Spearman rank) relationships between variables. Legend indicates strength of correlation coefficient (ranging from black/value of 1: high correlation to white/value of 0: weak correlation). Sample RH50, which originated from the upper conduit and thus is considered a subsurface sample, is not included in these matrices.

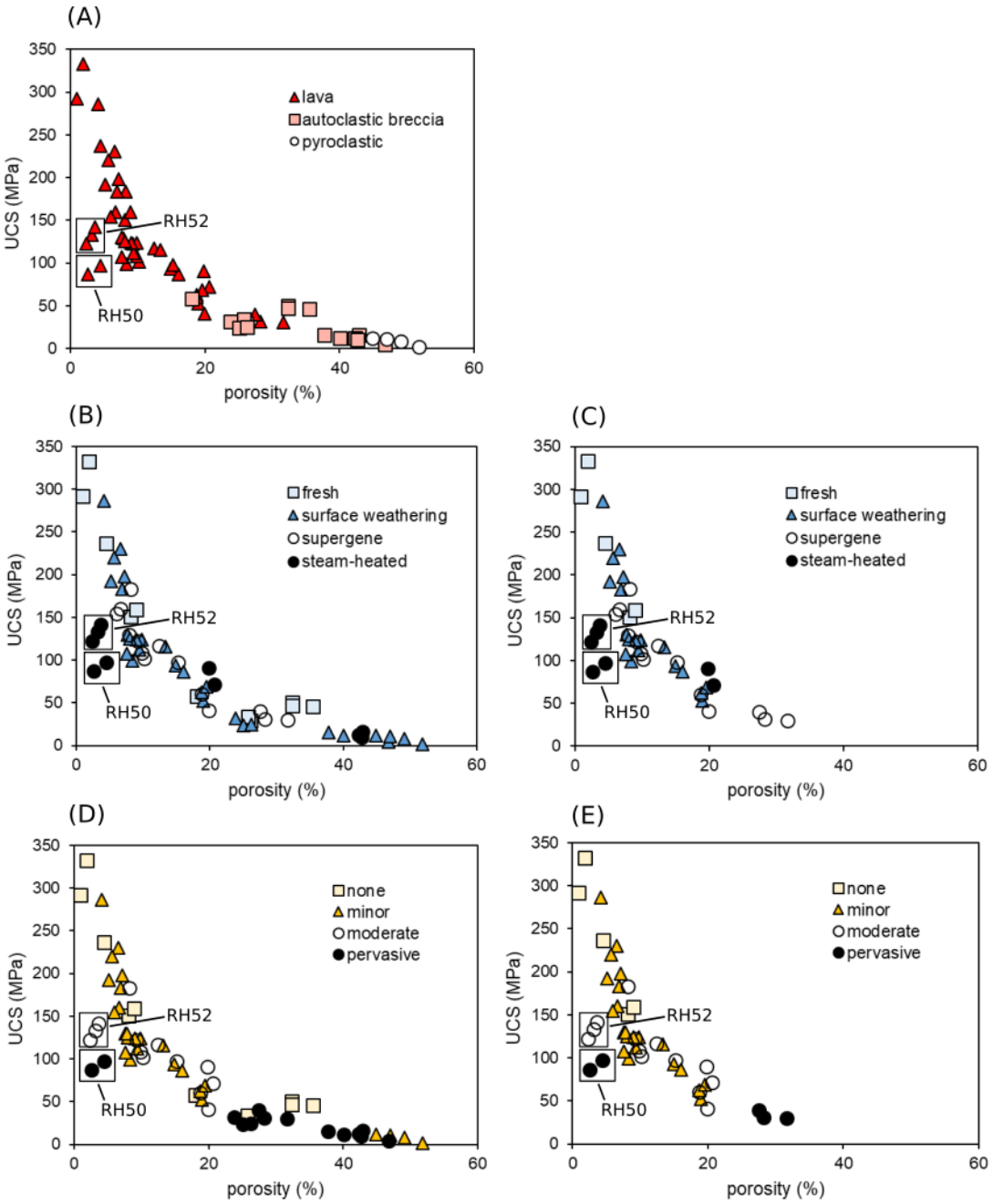


**Figure 6**. Porosity vs. uniaxial compressive strength (UCS) of all tested specimens, split into (A) lithology (all samples), (B) weathering/alteration mineralogy (all samples), (C) weathering/alteration mineralogy (lava rocks only), (D) pervasiveness of weathering/alteration (all samples), and (E) pervasiveness of weathering/alteration (lava rocks only). Porosity-UCS trend outliers RH50 and RH52 are discussed in the text.

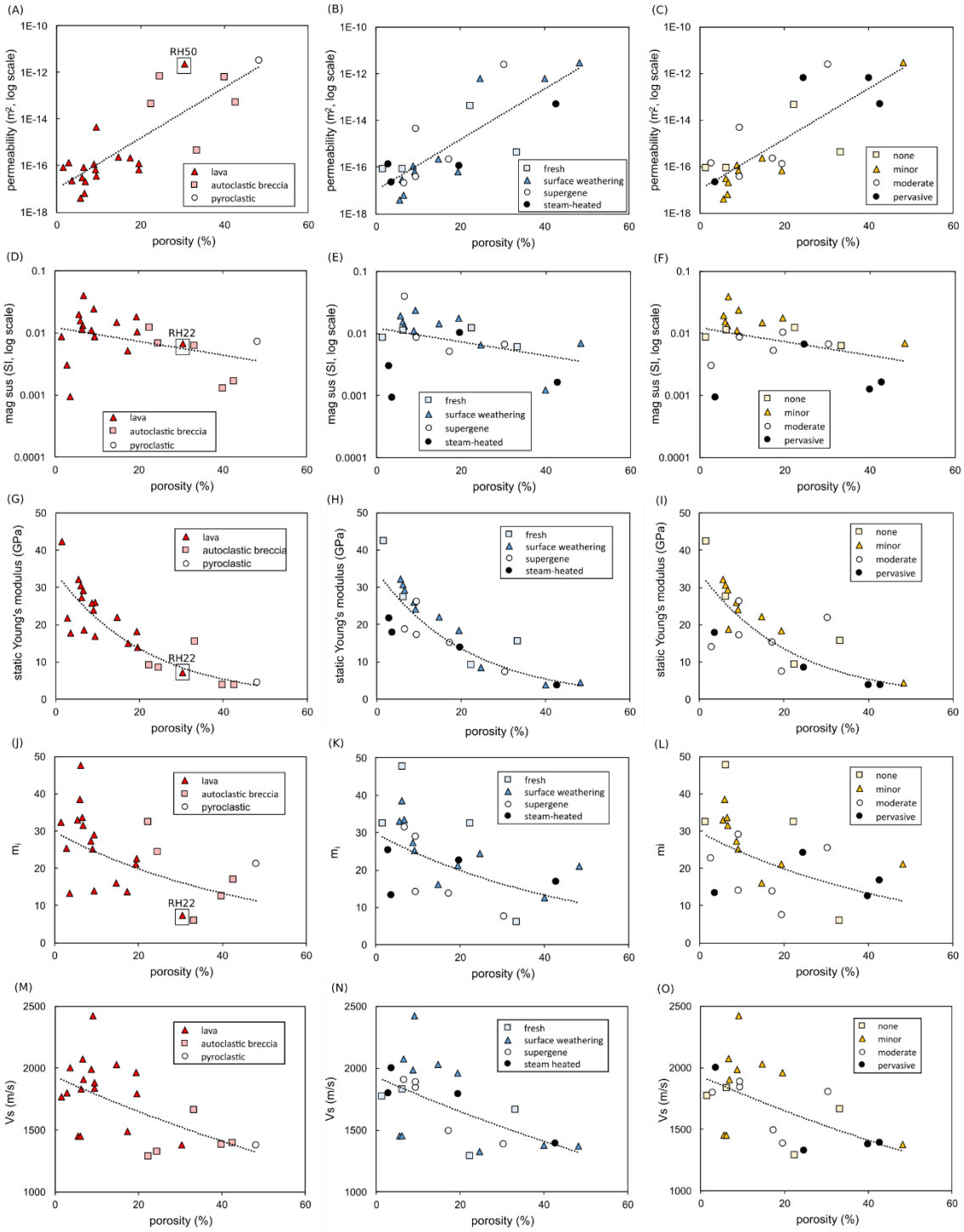


**Figure 7**. Relations of averaged block properties vs. averaged block porosity, split into columns according to lithology, weathering/alteration type, and weathering/alteration pervasiveness. (A-C) Porosity vs. permeability. (D-F) Porosity vs. magnetic susceptibility. (G-I) Porosity vs. static Young's modulus. (J-L) Porosity vs. Generalized Hoek-Brown failure criterion intact rock constant $m_i$. (M-O) Porosity vs. Vs. Outliers RH50 and RH22 in lithology graphs are discussed in the text.

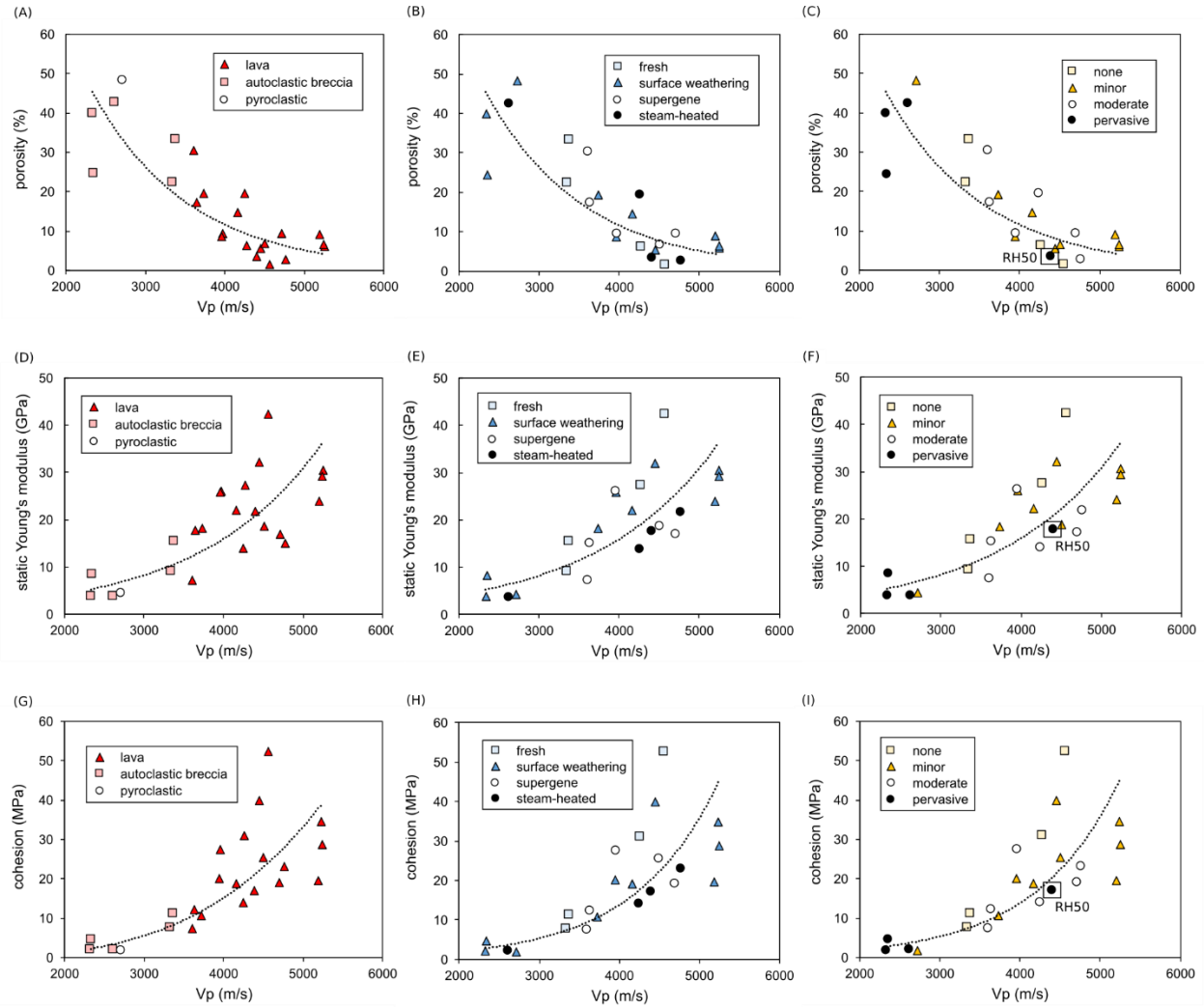


**Figure 8.** Relations of averaged block properties vs. averaged block P-wave velocity (Vp), split into columns according to lithology, weathering/alteration type, and weathering/alteration pervasiveness. (A-C) Vp vs. porosity. (D-F) Vp vs. static Young's modulus. (G-I) Vp vs. cohesion. Outlier RH50 in weathering/alteration pervasiveness graphs is discussed in the text.

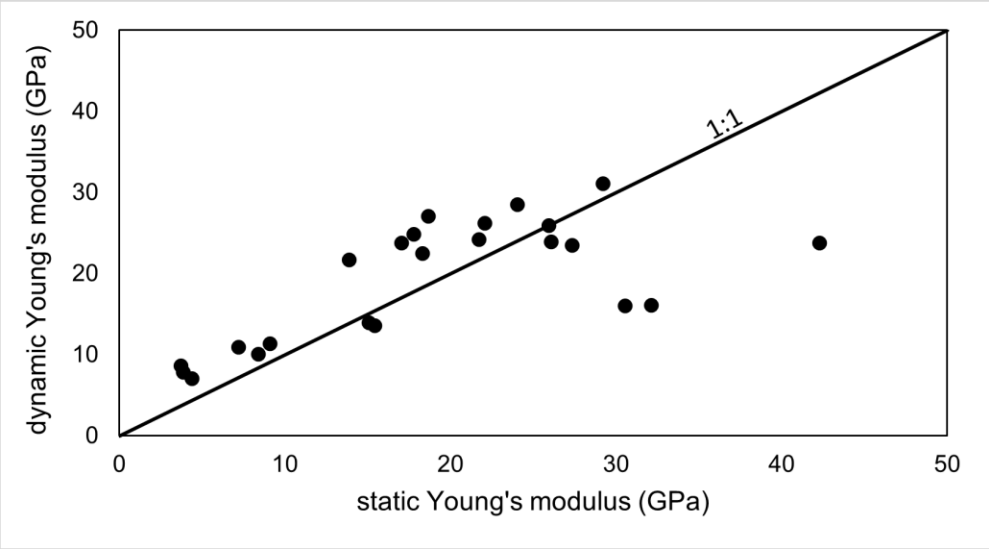


**Figure 9.** Static vs. dynamic Young's modulus values. Dynamic Young's modulus values tend to be higher than static Young's modulus, although more stiff material (values > 25 GPa) tends to have higher static Young's modulus values

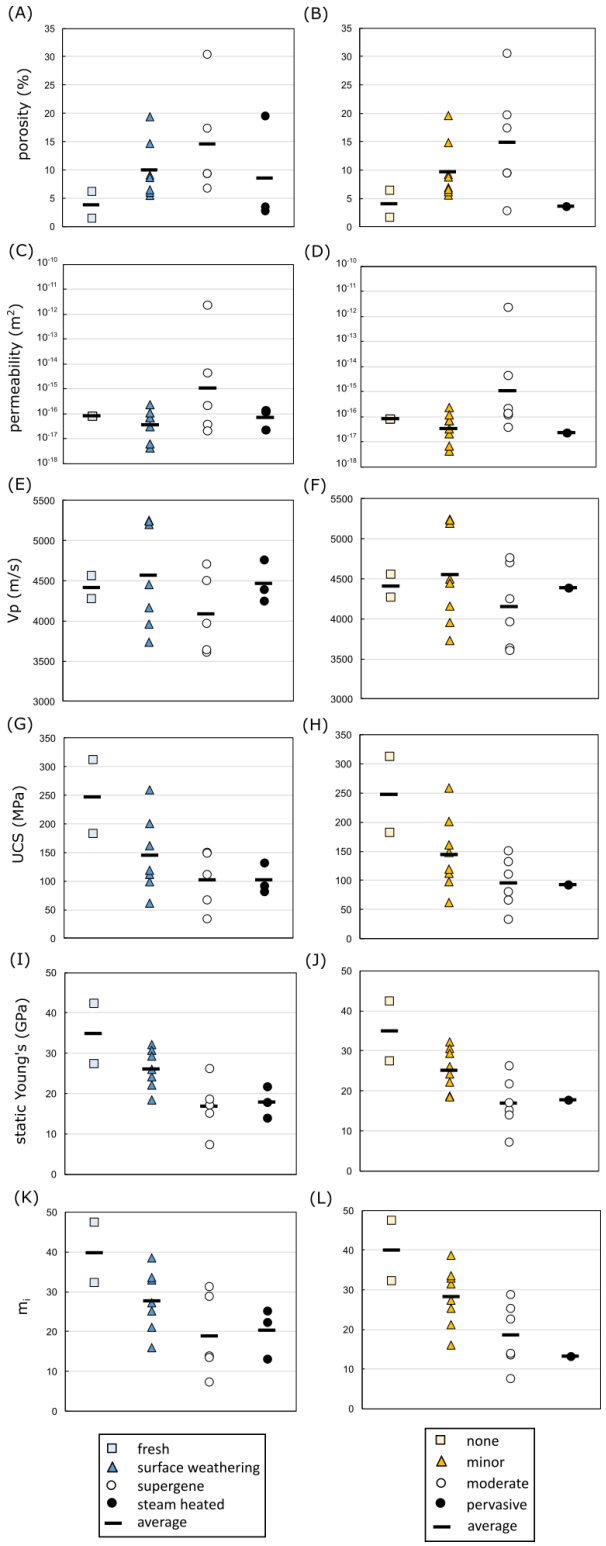


**Figure 10**. Averaged physical and mechanical properties of lava rocks only vs. alteration type and alteration pervasiveness for (A-B) porosity, (C-D) permeability, (E-F) P-wave velocity (Vp), (G-H) uniaxial compressive strength (UCS), (I-J) static Young's modulus, and (K-L) Generalized Hoek-Brown failure criterion intact rock constant $m_i$.

## Tables

**Table 1.** Location, geologic formation, and geologic member of samples used in this study. A description of the formations and members can be found in (Townsend et al., 2017). Undiff= undifferentiated.

| No. | Block | Location | UTM East | UTM North | Formation | Member |
|---|---|---|---|---|---|---|
| 1 | RH2 | Tukino | 379236.35 | 5651000.51 | Mangawhero | Horonuku |
| 2 | RH2b | Tukino | 379236.35 | 5651000.51 | Mangawhero | Horonuku |
| 3 | RH4 | Tukino | 377566.73 | 5651595.04 | Whakapapa | Iwikau |
| 4 | RH5 | Tukino | 377562.62 | 5651602.30 | Whakapapa | Iwikau |
| 5 | RH6 | Tukino | 377585.29 | 5651575.89 | Whakapapa | Iwikau |
| 6 | RH8 | Tukino | 377853.39 | 5651625.96 | Mangawhero | Horonuku |
| 7 | RH9 | Tukino | 378333.06 | 5651763.10 | Whakapapa | Iwikau |
| 8 | RH10 | Tukino | 380579.03 | 5650771.93 | Wahianoa | Wahinoa undiff |
| 9 | RH11 | Tukino | 380602.15 | 5650782.10 | Wahianoa | Wahinoa undiff |
| 10 | RH14 | Turoa | 371062.95 | 5646926.92 | Mangawhero | Makotuku |
| 11 | RH15 | Turoa | 373905.69 | 5649405.62 | Late Quaternary tephra | Late Quaternary undiff |
| 12 | RH16 | Turoa | 373838.72 | 5649332.31 | Mangawhero | Waitonga |
| 13 | RH17 | Turoa | 372410.37 | 5647578.84 | Mangawhero | Makotuku |
| 14 | RH17b | Turoa | 372410.37 | 5647578.84 | Mangawhero | Makotuku |
| 15 | RH19 | Whakapapa | 375835.14 | 5655487.92 | Whakapapa | Iwikau |
| 16 | RH21 | Whakapapa | 376462.30 | 5655607.92 | Te Herenga | Te Herenga undiff |
| 17 | RH22 | Whakapapa | 376402.26 | 5655448.21 | Te Herenga | Te Herenga undiff |
| 18 | RH28 | Whakapapa | 376323.48 | 5654474.1 | Te Herenga | Te Herenga undiff |
| 19 | RH38 | Tukino | 377584.94 | 5650878.81 | Wahianoa Fmt | Wahinoa undiff |
| 20 | RH42b | Tukino | 377544.95 | 5650936.57 | Whakapapa | Crater Lake |
| 21 | RH50 | -- | -- | -- | -- | 95/96 ejecta |
| 22 | RH52 | Crater lake | 376056.55 | 5650793.09 | Whakapapa | Crater Lake |
| 23 | RH52b | Crater lake | 376019.24 | 5650747.06 | Whakapapa | Crater Lake |

**Table 2**. Weathering/alteration category and associated mineral assemblages of collected sample blocks.

| Category | Mineralogy | Occurrence and origin | Blocks |
|---|---|---|---|
| Fresh | Primary (pyroxene, plagioclase, titanomagnetite) | Volcanic processes, minor surface weathering and/or oxidation | RH17, RH17b, RH19, RH42b |
| Surface weathering (weathered rim) | Primary and chemically weathered including smectites | Weathering of primary volcanic rocks with various percentages of primary (typically interior of sample) to weathered or oxidized (typically exterior/crust of sample) material | RH2, RH2b, RH4, RH5, RH6, RH8, RH9, RH10, RH15, RH16 |
| Supergene (argillic) | Phyllosilicates, jarosite, Fe oxides | Develops at <40°C through weathering and oxidation of sulfide-bearing rocks in atmospheric conditions | RH14, RH11, RH21, RH22, RH52b |
| Steam-heated (intermediate to advanced argillic) | Alunite, jarosite, opal, pyrite, Fe oxides, phyllosilicates, sulfur | Develops at <120°C near the water table and in the shallowest epithermal environment through alteration by steam-heated acid-sulfate waters | RH28, RH38, RH50, RH52 |

**Table 3.** Descriptions and average physical and mechanical laboratory results for each sample block.

| No | Block | Volcanic lithogloy | Mineral phases | Weathering/alteration category (see Table 2) | Extent of weathering/alteration | Magnetic susceptibility | Density (kg/m$^3$) | Porosity (%) | Permeability (m$^2$) | Vp (m/s) | Vs (m/s) | UCS (MPa) | Static Young's modulus (GPa) | $m_i$ | Friction angle (°) | Cohesion (MPa) |
|---|---|---|---|---|---|---|---|---|---|---|---|---|---|---|---|---|
| 1 | RH2 | lava | minor phyllosilicate and Fe oxidation | surface weathering | minor | 0.0155 | 2361 | 14.7 | 2.23E-16 | 4160 | 2029 | 98.38 | 22.07 | 16.08 | 47.87 | 18.89 |
| 2 | RH2b | lava | minor phyllosilicate and Fe oxidation | surface weathering | minor | 0.0221 | 2652 | 5.59 | 4.03E-18 | 4450 | 1452 | 258.14 | 32.13 | 32.97 | 54.36 | 39.89 |
| 3 | RH4 | autoclastic breccia | goethite, minor phyllosilicate | surface weathering | pervasive | 0.0072 | 2077 | 24.62 | 6.51E-13 | 2346 | 1325 | 26.81 | 8.4 | 24.27 | 51.72 | 4.6 |
| 4 | RH5 | lava | goethite, minor phyllosilicate | surface weathering | minor | 0.017 | 2595 | 6.07 | 3.06E-17 | 5246 | 1450 | 161.08 | 30.56 | 38.57 | 55.64 | 28.61 |
| 5 | RH6 | autoclastic breccia | minor phyllosilicate | surface weathering | pervasive | 0.0018 | 1722 | 39.95 | 6.19E-13 | 2329 | 1377 | 10.54 | 3.86 | 12.47 | 45.3 | 2 |
| 6 | RH8 | lava | geothite, minor phyllosilicate | surface weathering | minor | 0.0202 | 2228 | 19.45 | 6.65E-17 | 3731 | 1962 | 61.26 | 18.3 | 21.19 | 50.49 | 10.54 |
| 7 | RH9 | lava | geothite, minor phyllosilicate | surface weathering | minor | 0.0258 | 2517 | 9.14 | 6.65E-17 | 5193 | 2424 | 111.65 | 24.03 | 25.17 | 52.05 | 19.61 |
| 8 | RH10 | lava | jarosite, geothite and minor phyllosilicate (kaolinite) | surface weathering | minor | 0.0196 | 2569 | 6.59 | 6.26E-18 | 5241 | 2074 | 200.42 | 29.2 | 33.52 | 54.49 | 34.6 |
| 9 | RH11 | lava | geothite, Al and Fe rich phyllosilicate (kaolinite), and minor jarosite | supergene | moderate | 0.0062 | 2505 | 9.44 | 3.62E-17 | 4706 | 1836 | 110.72 | 17.04 | 28.87 | 53.24 | 18.93 |
| 10 | RH14 | lava | minor phyllosilicate, ferrihydrite and Fe oxidation | supergene | moderate | 0.0109 | 2425 | 9.44 | 4.33E-15 | 3963 | 1883 | 150.23 | 26.09 | 14 | 46.49 | 27.36 |
| 11 | RH15 | pyroclastic (scoria) | fresh rock with minor phyllosilicate and Fe oxidation | surface weathering | minor | 0.01 | 1372 | 48.25 | 2.98E-12 | 2715 | 1373 | 7.79 | 4.39 | 21.05 | 50.43 | 1.75 |
| 12 | RH16 | lava | fresh rock with minor phyllosilicate and Fe oxidation | surface weathering | minor | 0.0118 | 2440 | 8.73 | 1.10E-16 | 3955 | 1987 | 118.87 | 25.93 | 27.29 | 52.75 | 20.12 |
| 13 | RH17 | lava | fresh rock with minor Fe oxides | fresh | none | 0.0114 | 2521 | 6.32 | 8.02E-17 | 4271 | 1829 | 182.19 | 27.35 | 47.58 | 57.27 | 30.98 |
| 14 | RH17b | lava | fresh rock with minor Fe oxides | fresh | none | 0.0097 | 2623 | 1.57 | 8.02E-17 | 4563 | 1768 | 312.42 | 42.3 | 32.32 | 54.19 | 52.43 |
| 15 | RH19 | autoclastic breccia | fresh rock with minor phyllosilicate and Fe oxidation | fresh | none | 0.0125 | 2166 | 22.46 | 4.20E-14 | 3342 | 1287 | 40.48 | 9.1 | 32.36 | 54.2 | 7.58 |
| 16 | RH21 | lava | goethite, Fe-rich phyllosilicate and minor jarosite | supergene | minor | 0.0431 | 2668 | 6.77 | 2.06E-17 | 4503 | 1904 | 147.8 | 18.66 | 31.41 | 53.95 | 25.45 |
| 17 | RH22 | lava | jarosite, ferrihydrite, and minor Fe-rich phyllosilicate | supergene | moderate | 0.007 | 1985 | 30.43 | 2.33E-12 | 3607 | 1380 | 33.8 | 7.21 | 7.44 | 39.61 | 7.45 |
| 18 | RH28 | autoclastic breccia | montmorillonite, geothite, pyrite, quartz, and minor kaolinite | steam-heated | pervasive | 0.0027 | 1661 | 42.72 | 4.93E-14 | 2614 | 1394 | 12.69 | 3.72 | 16.84 | 48.32 | 2.05 |
| 19 | RH38 | lava | geothite, pyllosilicate, pyrite, quartz, and minor jarosite | steam-heated | moderate | 0.0102 | 2416 | 19.61 | 1.18E-16 | 4249 | 1791 | 81.03 | 13.89 | 22.49 | 51.04 | 14.06 |
| 20 | RH42b | autoclastic breccia | geothite, jarosite | fresh | none | 0.0061 | 1826 | 33.35 | 4.11E-16 | 3374 | 1661 | 47.71 | 15.43 | 5.93 | 36.93 | 11.12 |
| 21 | RH50 | lava (block) | alunite, jarosite, sulfur, and minor geothite, phyllosilicate (e.g. kaolinite, hallosite) | steam heated | pervasive | 0.0009 | 2292 | 3.64 | 2.19E-17 | 4395 | 2001 | 91.98 | 17.77 | 13.29 | 45.96 | 17.07 |
| 22 | RH52 | lava | goethite, minor sulfur, barite, phyllosilicate, pyrite, quartz and minor jarosite | steam-heated | moderate (primarily outer 6 mm) | 0.0103 | 2650 | 2.84 | 1.35E-16 | 4765 | 1797 | 132.47 | 21.74 | 25.25 | 52.07 | 23.04 |
| 23 | RH52b | lava | ferrihydrite, minor phyllosilicate | supergene | moderate | 0.0073 | 2285 | 17.38 | 2.10E-16 | 3638 | 1491 | 66.24 | 15.07 | 13.6 | 46.2 | 12.21 |

**Table 4.** Triaxial compressive strength results for varying confining pressures.

| *confining → pressure (MPa)* | *2* | *3* | *5* | *10* | *15* | *20* | *22* | *25* |
|---|---|---|---|---|---|---|---|---|
| Block | Peak stress (MPa) for a given confining pressure | | | | | | | |
| RH2 | | | 137 | 138 | | 231 | | |
| RH2b | | | 310 | 369 | | | | |
| RH4 | 46 | 46 | 73 | | | | | |
| RH5 | | | 279 | 292 | | | | 459 |
| RH6 | 22 | 22 | 35 | | | | | |
| RH8 | | | 92 | 131 | 175 | | | |
| RH9 | | | 163 | 228 | | | 288 | |
| RH10 | | | 273 | 344 | | | | 479 |
| RH11 | | | 178 | 193 | | | | 338 |
| RH14 | | | 176 | 201 | | | | 302 |
| RH15 | 25 | 30 | 65 | | | | | |
| RH16 | | | 148 | 239 | | | | 236 |
| RH17 | | | 273 | 327 | | | | 536 |
| RH17b | | | 322 | 495 | | | | 598 |
| RH19 | | 79 | 87 | 147 | | | | |
| RH21 | | | 212 | 273 | | | | 396 |
| RH22 | 49 | 43 | 55 | | | | | |
| RH28 | 25 | 45 | 37 | | | | | |
| RH38 | | | 128 | 158 | | 231 | | |
| RH42b | | 61 | 98 | 81 | | | | |
| RH50 | | | 114 | 154 | | 200 | | |
| RH52 | | | 253 | 230 | | | | 345 |
| RH52b | | | 82 | 134 | 146 | | | |